



**AIAA 92-0625**

**A Systematic Experimental and Computational  
Investigation of a Class of  
Contoured Wall Fuel Injectors**

**I. A. Waitz, F. E. Marble, and E. E. Zukoski**

**California Institute of Technology  
Pasadena, California 91125**

**30th Aerospace Sciences  
Meeting & Exhibit  
January 6-9, 1992 / Reno, NV**

# A SYSTEMATIC EXPERIMENTAL AND COMPUTATIONAL INVESTIGATION OF A CLASS OF CONTOURED WALL FUEL INJECTORS

Ian A. Waitz,\* Frank E. Marble,\*\* and Edward E. Zukoski\*\*\*  
*California Institute of Technology, Pasadena, California 91125*

## Abstract

The performance of a particular class of fuel injectors for scramjet engine applications is addressed. The contoured wall injectors were aimed at augmenting mixing through axial vorticity production arising from interaction of the fuel/air interface with an oblique shock. Helium was used to simulate hydrogen fuel and was injected at Mach 1.7 into a Mach 6 airstream. The effects of incoming boundary layer height, injector spacing, and injectant to freestream pressure and velocity ratios were investigated. Results from three-dimensional flow field surveys and Navier-Stokes simulations are presented. Performance was judged in terms of mixing, loss generation and jet penetration.

Injector performance was strongly dependent on the displacement effect of the hypersonic boundary layer which acted to modify the effective wall geometry. The impact of the boundary layer varied with injector array spacing. Widely-spaced arrays were more resilient to the detrimental effects of large boundary layers. Strong dependence on injectant to freestream pressure ratio was also displayed. Pressure ratios near unity were most conducive to loss-effective mixing and strong jet penetration. Effects due to variation in mean shear associated with non-unity velocity ratios were found to be secondary within the small range of values tested.

## Nomenclature

$\bar{A}$	injectant to freestream area ratio
$C_{He}$	helium mass fraction
$h_i$	height of injection plane
$\bar{M}$	injectant to freestream molecular weight ratio
$\bar{m}$	injectant to freestream mass flux ratio
$M$	Mach number
$p$	static pressure
$P_t$	pitot pressure

---

\* Graduate Student in Aeronautics, now Assistant Professor of Aeronautics and Astronautics, Massachusetts Institute of Technology, Member AIAA

\*\* Professor of Mechanical Engineering and Jet Propulsion, Emeritus, Fellow AIAA

\*\*\* Professor of Mechanical Engineering and Jet Propulsion, Fellow AIAA

$p_0$	stagnation pressure
$\bar{p}$	injectant to freestream static pressure ratio
$Re$	Reynolds number
$T$	static temperature
$\bar{T}$	injectant to freestream static temperature ratio
$T_0$	stagnation temperature
$S$	entropy
$\bar{v}$	injectant to freestream velocity ratio
$w_i$	width of injection plane
$x$	streamwise, axial coordinate
$\bar{x}$	non-dimensional distance downstream of the injection plane, $x/h_i$
$y$	cross-stream coordinate
$\bar{y}$	non-dimensional cross stream coordinate, $y/h_i$
$z$	vertical coordinate
$\bar{z}$	non-dimensional vertical coordinate, $z/h_i$
$\bar{z}_j$	jet lift-off height, helium mass flux center normalized by $h_i$
$\alpha_c$	geometric compression angle of upper ramp surface
$\alpha_e$	geometric expansion angle of channel between injector ramps
$\delta$	boundary layer height
$\delta^*$	boundary layer displacement thickness
$\bar{\delta}$	non-dimensional boundary layer height, $\delta/h_i$
$\rho$	density
$\bar{\rho}$	injectant to freestream density ratio
$\phi$	equivalence ratio
$\vec{\omega}$	vorticity vector

## Introduction

Development of air-breathing propulsion for flight at hypersonic Mach numbers has required the introduction of new concepts for mixing gaseous hydrogen fuel with a supersonic airstream. Fuel injector designs for this regime must meet exacting criteria. For combustor lengths of practical interest, through-flow speeds on the order of 10,000 ft/s dictate that molecular-scale mixing be completed in less than one millisecond. Further a significant component of the momentum of the injectant must be directed parallel to the freestream to augment thrust. A precarious balance between drag and mixing augmentation must be achieved.

A variety of injection schemes have been, and are currently being tested to meet these requirements. One general class of injector geometries is termed here "contoured wall injectors". These provide for conditioning of the flow field into which the fuel is injected by variation in wall geometry.

The injectors investigated in this study belong to this class. They were designed for mixing augmentation to result from intersection of the fuel/air interface with an oblique shock such that axial vorticity is produced. Other contoured wall injectors not designed specifically for shock-enhancement, but employing sweep of the injector side walls to enhance axial vorticity production of been studied at great length at NASA Langley Research Center<sup>1-5</sup> and elsewhere.<sup>6-7</sup> Many of the conclusions of this study are applicable to these geometries as well. Both higher mixing and higher flow losses have been found for addition of sweep to the injector side walls. In contrast to contoured wall schemes, transverse wall injection relies upon injectant interaction with the freestream to generate convective mixing. Studies of low-angled, transverse injection have been made where gaseous fuel is injected from ports in a flat combustor wall at angles of 10 to 30 degrees relative to the freestream flow direction.<sup>8-11</sup> A additional means for augmenting mixing involves preconditioning the fuel through various turbulizing and vorticity generating measures within the injector ports themselves.<sup>12-14</sup> Non-axisymmetric nozzle geometries have also been considered and were shown to enhance mixing.<sup>15,16</sup> It is likely that some combination of these methods/schemes may be required to meet the difficult requirements for hypersonic, air-breathing propulsion.

#### Shock-Enhanced Mixing

The baroclinic source term in the vorticity equation,

$$\rho \frac{D(\vec{\omega})}{Dt} = \frac{1}{\rho^2} \nabla \rho \times \nabla p$$

shows the dependence of vorticity production on the cross product of the gradients in pressure and density. Vorticity is formed at any point where the gradients are non-parallel. Thus, intersection of a shock with a non-parallel fuel/air density gradient will cause a baroclinic generation of vorticity.

Investigations of flow morphology associated with unsteady shock interaction with two-dimensional density inhomogeneities were carried out by Haas and Sturtevant.<sup>17</sup> Further work by Marble, Hendricks and Zukoski<sup>18</sup> and later by Yang<sup>19</sup> was directed towards understanding the mixing produced by such an interaction. These studies advanced the unsteady, two-dimensional problem of a shock passage over a circle of light gas imbedded in air as a canonical model for the three-dimensional steady problem of passage of a column of hydrogen fuel through an oblique shock wave. The studies showed that a strong increase in interfacial surface area resulted from the action of the vorticity deposited along the fuel/air interface as a result of shock-impingement.

#### The Contoured Wall Fuel Injector

This earlier work prompted efforts to design a realistic scramjet injection scheme in which shock-generated streamwise vorticity could be used to augment the mixing process. A geometry was presented by Marble *et al.*<sup>20</sup> and is shown in Figure 1. The scheme consists of alternate compression ramps and expansion troughs. The end of each of the ramps houses a nozzle discharging the injectant. Fuel is injected parallel to the freestream velocity vector to provide full utilization of the momentum of the injectant. An oblique shock is formed when the flow in the channels between the injectors is turned parallel to the freestream. This shock is drawn on the side view of Figure 1. It was intended that impingement of this shock upon the density gradient existing between the light fuel and the air, would

generate axial vorticity via baroclinic torque, and provide enhanced mixing.

A broad study was undertaken to evaluate the performance of these injectors in terms of mixing, jet penetration, losses, and heating considerations.<sup>21</sup> This work included both experiments at the NASA Langley High Reynolds Number Mach 6 Wind Tunnel, and numerical simulations using a three-dimensional Navier-Stokes solver. A description of the flow phenomena associated with a single geometric configuration subject to fixed injectant and freestream conditions was presented by Waitz, Marble and Zukoski.<sup>22</sup> Of primary interest in these tests was the definition of salient flow field features, particularly those relating to shock-enhancement of the mixing process. Temporally-resolved, planar Rayleigh scattering data were presented to impart a qualitative knowledge of the role and importance of unsteady components of the flow field. The test case presented in reference 22 will be used in this discussion as a baseline case against which comparisons are made to determine the effects of various parameter variations.

#### Scope of the Investigation

The goal of the work described here was to evaluate the influences of injector spacing, incoming boundary layer height, and injectant to freestream pressure and velocity ratios on the performance of the contoured wall injectors. All of the injectors studied had 2x1 rectangular injection planes ( $h_i = 2w_i$ ) and were characterized by the expansion and compression angles of the ramps ( $\alpha_e$  and  $\alpha_c$ ), and the spacing between the injectors. For the results presented,  $\alpha_e = \alpha_c = 4.76^\circ$ . Axes and pertinent geometrical parameters are detailed on the drawing of Figure 1. The barred quantities ( $\bar{x}$ ,  $\bar{y}$  and  $\bar{z}$ ) denote distances normalized by the height of the injection plane,  $h_i$ . Two scales of injectors were tested. These will be termed "full-scale" ( $h_i = 1.0$  in.) and "half-scale" ( $h_i = 0.5$  in.). The former allowed detailed surveying while the latter provided information at larger non-dimensional distances from the injection plane. The two scales also allowed a broader range of boundary layer heights to be investigated.

The ranges of the various parameters investigated are listed below. Freestream conditions corresponded to  $M = 6$ , with horizontal helium injection at  $M = 1.7$ .

#### Injector array spacing

Two array spacings were investigated. For the "narrowly-spaced" array, trough width was equal to the ramp width. The "widely-spaced" geometry was such that the trough width was equal to approximately three times the width of the injection plane.

#### Boundary layer

Turbulent boundary layers with heights between  $\bar{\delta} = 0.2$  and  $0.7$  were investigated experimentally. ( $\bar{\delta}$  is the height of the boundary layer normalized by the height of the injection plane.) Numerically, simulations were conducted for  $\bar{\delta} = 0.2$  and  $\bar{\delta} = 1.0$ . A free-slip boundary condition was also modelled numerically.

#### Pressure ratio

Injectant to freestream pressure ratios of  $\bar{p} = 0.4, 1.0, 2.0$ , and  $4.0$  were studied computationally. Experiments were conducted for  $\bar{p} = 1.0$  and  $\bar{p} = 4.0$ .

#### Velocity ratio

Velocity ratios from  $\bar{v} = 1.12$  to  $\bar{v} = 1.36$  were tested experimentally. Simulations were run for  $\bar{v} = 0.8, 1.0$ , and  $1.2$ .

While a fully-populated, parametric test matrix might be desired to elucidate the coupling between various parameters, financial and time constraints dictated a sparser, more directed approach to the study. A crude assumption of parameter independence was applied to changes in the velocity and pressure ratios, in the interests of limiting the scale of the tests. Thus, one condition was fixed as the baseline configuration against which variations of a single parameter were compared. Parametric independence was not assumed for changes in boundary layer scale and injector spacing. Here both spacing and boundary layer height were changed simultaneously as the effects were strongly interdependent.

It is appropriate at this point to include some disclaimer concerning the applicability of conclusions based on these helium-air mixing studies to the problem of current engineering interest - that of combustion of hydrogen and air within a scramjet. Mixing studies are germane because even with combustor through-flow times of 1 ms, the characteristic chemical time-scales place this reaction in the mixing-rate dominated regime. However, in the classical sense, the reaction will not be mixing-rate controlled, and thus the current studies address only part of the problem. The less tractable problem where finite-rate chemistry is included must be studied (both experimentally and with numerical simulations) before confidence in performance estimates can be developed. Certainly no chemical forcing of the flow field associated with heat release will be represented in the current study.

A second restriction on the applicability of the results of this study is associated with the inadequate spatial and temporal resolution of both the experimental and numerical techniques. Direct measurement of molecular-scale mixing was precluded. Unless otherwise stated, referrals to mixing performance will be made within the bounds of spatial and temporal resolution associated with the various experimental and numerical techniques. References to 'large-scales' will imply characteristic lengths greater than  $1/5 h_i$ .

## **Experimental and Computational Apparatus and Methodology**

### **Experiments**

The tests were conducted in the NASA Langley High Reynolds Number Mach 6 Wind-Tunnel. The tunnel is an open-loop blowdown type facility, with a 42 in. long, 12 in. diameter circular test section. Stagnation conditions were  $p_0 = 1000$  psia, and  $T_0 = 246^\circ$  C. The static properties associated with these conditions were  $p = 0.63$  psia and  $T = -210^\circ$  C, with a freestream Reynolds number of  $15 \times 10^6/\text{ft}$ . The tunnel was equipped with a three-axis traverse and a helium supply system both designed by NASA personnel for these studies.

A modular wind-tunnel model allowed testing of a variety of injector configurations. The model was in the form of a "T" with a flat plate mounted on a center strut. The upper surface of the plate was used to model one interior wall of a scramjet combustion chamber. The flat plate extended 15 inches upstream of the start of the injector ramps. Boundary layer tripping was provided using normal air injection from an array of 0.020 in. diameter holes located 1 inch from the leading edge of the model. Downstream from the injectors, the flat plate extended 21 inches. The test surface was 7.625 inches wide. Plates were mounted on the sides of the model

to limit the influence of pressure disturbances below the plate on the test flow.

Three-dimensional surveys were the primary means used to investigate the flow field. Four rake-mounted probes were used: a cone static pressure probe, a pitot probe, a total temperature probe and a composition probe. Data collection was automated using a personal computer-based, data acquisition system.

Determination of gas composition was central in analyzing injector performance. The composition probe developed was based on the response of a hot-film anemometer probe in a binary gas mixture. The response can be expressed as a function of velocity, temperature, pressure and composition. A sample was withdrawn from the flow using a vacuum pump and allowed to pass over a hot-film sensor. Maintenance of sufficient mass flow and internal divergence of the sampling tip assured swallowing of the probe induced bow shock so that the sample obtained would not be subject to species separation.<sup>23-25</sup> After removal from the tunnel, the sample was temperature-fixed using an ice-bath. Velocity was fixed for given pressure, temperature and composition by choking the flow just downstream of the sensor. With these variables fixed, anemometer output was a function of only pressure and composition. Pressure was measured at the sensor location. Composition was determined from interpolation of a sensor output calibration for pressure and composition. The design and application of this device are presented in detail in reference 22. This apparatus allowed determination of helium mole fraction with less than  $\pm 3\%$  error throughout the envelope of experimental conditions ( $M = 6$  air at  $p_0 = 1000$  psia,  $T_0 = 246^\circ$  C, to  $M = 1.7$  helium at  $p_0 = 3.4$  psia,  $T_0 = -50^\circ$  C). Response time on the order of 1.5 seconds, combined with wind-tunnel run times of greater than one hour allowed detailed surveying of the injector flow field.

In addition to the surveys, surface static pressure measurements, and various flow visualization techniques were employed. These techniques included surface oil flow, time-mean Schlieren, time-resolved shadowgraph, and time-resolved planar Rayleigh scattering. The Rayleigh scattering was invaluable in imparting knowledge of the unsteady aspects of the flow field, and was a result of a collaborative effort with members of the Optical Spectroscopy Section of NASA Langley's Instrument Research Division. Details of the technique appear in references 21 and 22.

### **Computations**

A series of numerical simulations were conducted as a complement to the experimental investigation. The simulations were performed using the SPARK3D<sup>26,27</sup> code obtained from the Computational Methods Branch of NASA Langley Research Center. The code integrates the three-dimensional Navier-Stokes, energy and species continuity equations for a multiple species system with finite-rate chemistry. The code has become a workhorse for modelling both reacting and non-reacting flow about a variety of injector geometries (e.g. refs. 1-5 among others). For this study, the code was used in a non-reacting mode with  $M = 1.7$  helium injected into  $M = 6$  air to allow direct comparison with the experiments. The system of equations was advanced in time until convergence at steady state was obtained.

Typical domains consisted of 266,000 grid points. First order boundary conditions were applied to simulate an

infinite array of injectors in the crossflow plane, with an open flow boundary on the top of the domain.

A turbulence model was not applied. The decision to limit the scope of the computations to a laminar mixing model was based on the inability of current turbulence models to accurately reproduce complex mixing phenomena without significant 'tuning'. Application of an inappropriate turbulence model can influence the global solution in a manner which is difficult to resolve. Thus, the code was used only to capture large-scale kinematical processes. Fine-scale mixing was not simulated.

## Results

### The Baseline Configuration

As a starting point against which other conditions can be compared, the results for the baseline configuration will be summarized. A more detailed presentation of these results may be found in references 21 and 22. The baseline test configuration was characterized by a wide array spacing (trough width = 3 ramp widths), matched pressure ratio ( $p = 1.0$ ), a thin boundary layer ( $\delta = 0.2$ ), and  $\bar{v} = 1.33$  (for the experimental cases) or  $\bar{v} = 1.0$  (for the computational cases).

Results from a numerical simulation of the baseline case are shown in Figure 2. The plot contains contours of constant helium mass fraction at various planes downstream of the injection plane. The helium lifted completely from the surface by  $\bar{x} \approx 1$ . Downstream, helium mass fraction signatures are characteristic of interaction with a counter-rotating vortex pair. Axial vorticity from several sources coalesced to form this counter-rotating vortex pair. Importantly, the sense of the pair was such that it produced migration away from the wall, enhancing jet penetration. The cross-stream convection associated with the vorticity, enhanced mixing in the large scales. Preliminary work has shown that the dominant axial vorticity sources include: 1) baroclinic torque associated with shock-impingement, 2) local variation in cross-stream shear between the injectant and the airflow in the exit plane associated with the secondary flow due to the ramps, 3) turning of the vortex lines associated with the incoming wall boundary layer, and 4) further diffusive flux of vorticity associated with wall effects in the ramp region. Of these sources, shock-impingement and cross-stream shear were particularly effective in mixing the fluids as they assured seeding of axial vorticity directly on the helium/air density interface. These sources of axial vorticity will be characterized in greater detail in a subsequent publication.<sup>28</sup>

Experimentally obtained mass fraction and pitot pressure surveys are shown in Figures 3 and 4. These data were obtained from measurements of one symmetry plane on the full-scale model and have been mirrored about the plane  $\bar{y} = 0$  for purposes of presentation. The side walls of the ramp correspond to  $\bar{y} = \pm 0.25$ . Care must be taken in interpreting these and other plots shown so that credence is not given to sub-grid scale features. The experimental sampling grid has been overlaid on one of the plots of Figure 3.

An important aspect of the boundary flow is shown in the pitot pressure plots of Figure 4. The pressure gradients associated with expansion and compression of the ramp surfaces drove the majority of the incoming boundary layer flow into the troughs between the ramps. Of note is that a tongue of high momentum fluid was maintained in the

corner of the ramps. This allowed strong shock formation directly adjacent to the nozzle exit where it was required for impingement upon the fuel/air density gradients. It will be seen that this counter-intuitive result (initial expectations were for the corner region to contain the lowest momentum fluid) was not realized for all spacings and boundary layer heights.

One conclusion of the previous work was that the numerical simulations captured the essential large-scale kinematics displayed in the experiments. (Recall that no attempt was made to accurately model mixing in the fine-scales.) The above observation is valid only to the extent to which these scales were resolved. In particular, estimates of convective and diffusive transport showed that the detailed form of the time-mean helium signatures is likely to be misrepresented (in both the experiments and the computations), with the possibility existing for tightly-rolled spiral species gradients within the helium core. The extent to which these scales may have been dominated by turbulent processes was only addressed superficially. Temporally-resolved planar Rayleigh scattering data suggested that production of molecularly-mixed fluid would be dominated by the turbulent cascade process in the far field ( $\bar{x} > 10$ ). The influence that the large-scale vortical flow had on this process was not established.

### Bases for Comparison

Various measures of performance are discussed below. They relate to the following categories: mixing, loss generation, injectant penetration, and surface heating considerations.

#### *Decay of Maximum Helium Concentration*

One marker for time-mean mixing performance is the decay of maximum helium mass fraction downstream of the injectors,

$$C_{He-max} \text{ VS. } \bar{x}$$

This measure was tabulated from the composition probe measurements at each surveyed plane and is plotted in Figure 5 for the baseline case. It represents a bulk measure of the extent to which the injectant has mixed with the freestream. It is often heavily relied upon in grading injector performance due to the relative ease in obtaining the measure. It must be remembered that the measure is clouded by the influences of unsteadiness and spatial averaging and is of limited use in projecting combustion effectiveness.

#### *Mixedness Measure*

The numerical data allow more detailed analyses of mixing, but are still subject to the hindrances discussed above. Further, due to the limited scope of the computations with respect to fine-scale mixing, only qualitative comparisons were allowed with the experimental data. Direct quantitative comparisons were made between the simulations. Analysis of mixing was performed through determination of the fraction of total helium mass flux present in various concentrations at each axial station,

$$\frac{\dot{m}_{He}}{\dot{m}_{He-total}} \text{ VS. } C_{He} \text{ VS. } \bar{x}$$

This measure is displayed on both surface and contour plots in Figure 6 for the baseline case. Downstream from the injection plane, progressively larger percentages of the injected mass flux appear in the lower mass fractions. Three

characteristics of this progression were used as a basis for comparison with data from other numerical cases. The first of these is how rapidly the point was reached where there was no longer any pure helium in the flow field. This occurred at approximately  $\bar{x} = 15$  for the baseline case. The second, the extent to which the bulk mixing process continued to occur, is represented by the zero contour in the line plot. The line corresponds with the decay of maximum helium concentration plotted for the experimental results in Figure 5. Qualitatively, the behaviors of the two lines are similar. The third aspect of this mixedness data that was used for comparison with other numerical tests is the percent of helium mass flux present at the lower mass fractions where the mixture ratio would promote most active burning in a hydrogen/air reaction system. The level of mass flux occurring at  $c_{He} \leq 0.05$  was used as a measure of this. This level is indicated by the height of the lower edge of the carpet plot. By  $\bar{x} = 30$ , approximately 17% of the injected mass flux was below 5% mass fraction for the baseline computational case.

#### Interface Length

A second measure of mixing performance based on the numerical simulations is the variation in length of contours of constant mass fraction, with distance downstream of the injection plane,

$$\frac{L_{\alpha}(\bar{x})}{L_{\alpha}(\bar{x}=0)} \text{ vs. } c_{He} \text{ vs. } \bar{x}$$

Where  $L_{\alpha}$  corresponds to the length of a contour of helium mass fraction  $c_{He} = \alpha$ . This information relates the growth in time-mean interfacial surface area resulting from the cross-stream transport due to the axial vorticity. Growth of surface area is a necessary kinematical precursor to strong molecular-scale diffusive mixing. This measure suffers strongly from lack of spatial resolution and must be considered as a means for only rough quantitative comparisons between numerical data sets. For the baseline case the contour of  $c_{He} = 0.05$  grew to twice its initial length by  $\bar{x} = 10$ . This length was then maintained through counterbalancing of diffusion/resolution and convection.

#### Jet Penetration

The above measures are strongly limited by spatial and temporal averaging and are thus very weak measures of molecular mixing. Both the experiments and numerical simulations however, were very adept at predicting large-scale kinematical processes. This is evidenced by the comparison of helium jet lift-off height for the experiments and computations shown in Figure 7. This was calculated from the numerical data as the height of the helium mass flux center and approximated using the experimental data by calculating the height of the mass fraction center. (The approximation is valid due to generally concentric stratification of helium mass fraction about the mass flux center.<sup>21</sup>) The lift-off height is a measure of the bulk behavior of the helium after injection and was used as the primary measure of jet penetration. For  $\bar{x} > 20$ , a constant jet trajectory slope of 0.025 is displayed.

#### Fully-mixed Length

The ability to accurately measure/simulate large-scale injectant dynamics led to the development of a mixing measure which is less dependent on detailed mixing-rate data than the measures presented above. The measure involves considering the area into which the injectant must spread in order for the bulk mixture fraction to reach a desired equivalence ratio. The injectant to freestream area ratio,  $A$ , for a given equivalence ratio,  $\phi$ , may be expressed as a function of injectant to freestream temperature, pressure,

velocity, molecular weight, and stoichiometric mass flux ratios ( $T$ ,  $\bar{p}$ ,  $\bar{v}$ ,  $M$ , and  $\dot{m}_{st}$  respectively),

$$A = \frac{\phi \dot{m}_{st} \bar{T}}{\bar{p} M \bar{v}}$$

For representative scramjet operating conditions ( $\phi = 1.0$ ,  $T = 1/6$ ,  $\bar{p} = 1.0$ ,  $\bar{v} = 1.0$ ,  $M = 2/29$ , and  $\dot{m}_{st} = 0.03$ ) then  $A = 0.07$  and the injectant must expand into an area approximately fifteen times the exit area. As the area will be limited laterally by the symmetry planes of the injector array, the vertical extent of the area would correspond to  $\bar{z} = 4.0$  for the baseline geometry. For the freestream velocities of these tests (3000 ft/s), peak penetration of that order would be expected by  $\bar{x} \approx 60$ . For the conditions of this study with  $\phi = 1.0$ ,  $T = 2.5$ ,  $\bar{p} = 1.0$ ,  $\bar{v} = 1.33$ ,  $M = 4/29$ , and  $\dot{m}_{st} = 0.03$ , then  $A = 0.41$ . Less air would be required to be entrained by the helium jet. Use of this information as a measure of mixing requires the assumption that diffusive and turbulent processes will produce a 'homogeneous' mixture by the time the jet has penetrated into the specified area. Consideration of time-resolved Rayleigh data give support to this assumption for distances of 50 to 60 injector heights because of the dominance of turbulent mixing after  $\bar{x} = 10$ .

#### Losses

The above measures of injector performance focus on mixing effectiveness and jet behavior. It is important as well to grade various injectors and test conditions on a loss basis. The losses were evaluated by considering the entropy rise in the fluid as it passed through the computational domain. The entropy rise can be associated with two categories of losses: total pressure losses and mixing losses. The latter result from a change in partial pressure of two species as they are mixed. Consider two distinct gases in a box separated by a membrane. The entropy rise which results from removal of the membrane is

$$\Delta S = R_u \left[ n_1 \ln \left( \frac{V_1 \text{ final}}{V_1 \text{ initial}} \right) + n_2 \ln \left( \frac{V_2 \text{ final}}{V_2 \text{ initial}} \right) \right]$$

where  $R_u$  is the universal gas constant,  $n_i$  are the number of moles of each species, and  $V$  is the volume. In applying an entropy measure of propulsive losses it is important to separate from the total entropy rise, that part associated solely with mixing of the two species. The latter is only a loss in the thermodynamic sense not the propulsive one. (Consider red gas and blue gas with otherwise identical characteristics. Upon mixing in a duct, there is no change in propulsive potential, yet an entropy rise is realized.) Since the mass fraction at each point in the computational domain was known, the entropy rise due to mixing was calculated for each computational cell and removed from the total entropy rise to form a measure of propulsive losses.

The above bases for comparison along with close analysis of the flow field surveys and computational data sets were applied to each of the test configurations. For a presentation of each of these measures for each of the test configurations the reader is referred to reference 21. Presently only a skeleton of support will be given for the various conclusions.

#### Boundary Layer/Injector Spacing Effects

Early flow visualization results showed that injector performance was strongly dependent on the scale of the boundary layer entering the ramp region, and that this

dependence was influenced to a large extent by the spacing between the injector ramps. It was, in fact, this knowledge which led to a viscous numerical modelling of the flow field, rather than an Euler simulation. Four aspects of the boundary layer affect injector performance (in varying degrees): modification of effective wall geometry through displacement, the addition of shear to the mixing region, influence on axial vorticity production through turning of mean vorticity in boundary layer, and addition of unsteadiness to the mixing region. These effects were treated largely as they were manifested in the time-mean flow field, though some time-resolved, planar imaging data was collected.

Two boundary layer conditions were investigated experimentally: natural and tripped. (For both cases the boundary layer was turbulent prior to entrance into the ramp region.) For the tripped case, 80 psi total pressure air was injected from a boundary layer trip plate on the front of the model. The two conditions resulted in  $\delta = 0.2$  and  $0.35$  ( $\delta$  is the height of the boundary layer normalized by the height of the injection plane) for the full-scale models ( $h_i = 1.0$  in.) and  $\delta = 0.4$  and  $0.70$  for the half-scale models ( $h_i = 0.5$  in.). The nature and the scale of the boundary layer were determined from consideration of time-resolved shadowgraph images and time-mean flow surveys. No measurements were made to determine the magnitude of the fluctuations within the boundary layer. To support the above work, numerical simulations were conducted for free-slip boundary conditions ( $\delta = 0$ ), and for  $\delta = 0.2$ , and  $1.0$ .

Peak helium mass fractions for the natural boundary layer case were marginally higher than those obtained for the tripped cases. A plot of the decay of the maximum helium concentration in  $\bar{x}$  for both the full and half-scale models for the various boundary layer conditions is shown in Figure 8. The trend for more rapid decay of the time-mean values with increasing boundary layer height is displayed. This result is closely tied to the interaction of the unsteady structure within the boundary layer with the time-fluctuating component of the mixing field. Determination of the extent to which this represented increased mixing on the molecular scale was aided by consideration of the planar Rayleigh imaging results.<sup>21</sup> Typically, the jet appeared to have been subject to more large-scale, global deformation. This deformation was linked to the long wavelength oscillations present in the boundary layer. Locally, however, the scale and nature of the unsteady field on the boundary of the helium jet was similar to that for the natural boundary layer case. The implication is that the unsteady structure of the boundary layer did not act strongly to enhance mixing on the molecular scale. The small increase in time-mean mixing for the tripped boundary layer, displayed by the peak helium mass fraction decay (Figure 8), probably resulted from greater spatial averaging due to the global motion of the jet.

The displacement effects of the boundary layer were resolved with greater confidence since they involved predominantly the mean flow. For the  $\delta = 0.7$  case, flow surveys showed that the boundary layer filled the channels between the injector ramps to a much greater extent than seen for the thin boundary layer. Importantly though, a tongue of high momentum fluid was still maintained in the corner of the ramps, with the lowest momentum fluid collecting in the center of the troughs. The interaction was positive in that it allowed shock formation in the region adjacent to the injectant/freestream density gradients allowing baroclinic vorticity production. The presence of high momentum in the corners of the ramps was further evidenced by surface oil flow visualization. The oil tended

to collect in the center of the channels with the high momentum fluid scrubbing the oil from the surface in the corners of the ramps.

A similar positive interaction between the boundary layer and the ramp geometry did not occur for the narrow spacing injector arrays. Schlieren photographs showed no strong oblique shock appearing from the compression of the trough flow between the injection planes. This forecasted a decline in baroclinic vorticity production associated with the shock-impingement on density gradients. The cause for the absence of the shock was apparent in the time-mean flow field surveys. This data is shown in Figures 9 and 10 (half-scale model,  $\delta = 0.7$ ). The pitot pressure survey (Figure 10) shows the extent to which the troughs between the ramps were filled with the low momentum boundary layer fluid. The geometry was effectively modified due to the strong displacement effect of the hypersonic boundary layer. The helium mass fraction contours (Figure 9) show weaker vortical development and poorer jet lift-off than realized for the wider spacing. The effects on lift-off due to spacing are shown in Figure 11 for the various boundary layer conditions. The slope of the injectant trajectory for the narrow spacing is one-half that for the wide-spacing. For the narrow spacing  $\bar{z}_j = 0.8$  at  $\bar{x} = 26$ , while  $\bar{z}_j = 1.1$  at  $\bar{x} = 26$  for the wide spacing. The close proximity of the jets produced strong interaction between them. By  $\bar{x} = 13$  the jets fully merged, forming a thick layer of helium/air mixture along the surface of the wall. Considering the jets as simple counter-rotating vortices, it is clear as well that closer proximity will reduce migration rate away from the wall.

As with the wide spacing, imposition of the tripped boundary layer produced a slight increase in the bulk mixing efficiency as evidenced by the decay of maximum helium concentration plotted in Figure 12. Again, the extent to which this trend is representative of molecular-scale mixing is difficult to determine from the tests conducted. However, it is clear that on a macroscopic scale the change was minor.

Based on the weaker lift-off and vortical roll-up of the jet for the narrow spacing, a decline in bulk mixing effectiveness was expected. This was not the case, as shown in Figure 13. The decay of maximum helium mass fraction is plotted for both the narrow and wide spacing for the various boundary layer conditions. The wide spacing cases are represented with solid lines. Broken lines are used for the narrow spacing cases. While initially the levels for the narrow cases were higher than those for the corresponding boundary layer conditions for the wide spacing, the trend was reversed after  $\bar{x} = 10$ . Thus, globally, the time-mean mixing for the narrow geometry was better in the farfield. The manifestation of better mixing in the mean for the narrow spacing was probably due to the close interaction of the jets with the boundary layer. This interaction is evident in the  $\bar{x} = 8$  contour plot of pitot pressure in Figure 10 where the interaction of the neighboring counter-rotating vortex pairs produced a high pressure center between the jets. While the vorticity field was weaker, the close proximity of the jets to the boundary layer resulted in the boundary layer being interred into the vortex pair. The unsteadiness in the core of the jets which would result puts in question the accuracy of the time-mean maximum concentration data in representing the time-resolved flow for the narrow spacing. Due to time constraints, no time-resolved planar imaging was conducted for the narrow geometry. For the wide spacing case, the bulk of the low momentum boundary layer fluid existed between the helium jets, and the jets rose above the boundary layer before strong interaction occurred. Even



though farfield time-mean mixing was marginally better for the narrow geometry, considerations of jet penetration (presented below) suggest that the wide spacing is more effective in terms of overall injector performance as a result of the stronger and more complete lift-off displayed.

Numerical simulations were conducted primarily to elucidate the detrimental effects of the boundary layer displacement with respect to the baroclinic generation of vorticity. Simulations were computed for both the wide and narrow spacings at  $\delta = 0, 0.2$  and  $1.0$ . Two effects were noted in comparing the results of these simulations. The first of these was the increase in mean shear at the interface provided by increasing boundary layer scale. This increased the size of the jet cross-sections through a broadening of the species gradient at the jet/freestream interface. The second effect was the progressively slower convective development of the jet with increasing boundary layer scale. Similar effects occurred for the narrow spacing geometry. Most notable in this portion of the study was the strong vortical development for the case of inviscid boundary conditions for the narrow spacing (Figure 14). That this development was not apparent for the case of the  $\delta = 0.2$  boundary layer (shown in Figure 15), shows the sensitivity of the narrow geometry to even thin boundary layers. For the narrow geometry, effectively more low momentum fluid per cross stream area occurred in the troughs. This preponderance of low momentum fluid did not allow shock formation for impingement upon density gradients in the mixing region, and reduced secondary flow associated with the ramps, both strong axial vorticity sources. The effect was minimized for the wide spacing because of positive interaction of the boundary layer flow with ramp-generated pressure gradients.

Analysis of the mixing performance for the various spacings in response to the different boundary layer thicknesses was provided by mixedness measure plots similar to Figure 6. Three aspects of these plots were recognized as indicators of effectiveness: the distance required for disappearance of pure helium in the flow field, the rate and extent of the decay of maximum helium concentration, and the percent of total helium mass flux occurring at  $c_{He} < 0.05$ . On all three bases, and for all boundary layer cases, the performance of the wide spacing was superior to that of the narrow spacing. Typically, the amount of helium appearing at  $c_{He} < 0.05$  for the wide cases was twice that for the narrow cases by  $\bar{x} = 30$ . Performance degraded similarly with increasing boundary layer height. The  $\delta = 1.0$  tests produced half as much  $c_{He} < 0.05$  fluid as the  $\delta = 0.2$  tests for both geometries. The analysis of contour lengths for the various cases also showed better performance for the widely-spaced injector array with contour lengths at  $c_{He} = 0.05$  typically at  $1.5$  to  $2.0$  times the initial length while similar interface lengths for the narrow spacing occurred at  $1.0$  to  $1.5$  times the same initial contour length.

A final consideration with respect to the spacing between the injectors is the freestream area required for the injectant to mix into, to provide a desired equivalence ratio. It was shown that for a representative scramjet operating condition an injectant to freestream area ratio of  $A = 0.07$  would be required for mixing to the stoichiometric hydrogen mass fraction. For the wide spacing, this area would extend to  $\bar{z} = 4.0$ . Due to the lateral confinement of the jets in the narrow spacing array, similar performance would require extension of the vertical scale of the area to  $\bar{z} = 8.0$ . Penetration of this order is not expected for the narrow spacing (within domains of interest for scramjet applications). It should not be concluded however, that in general the narrow spacing is

an ineffective configuration. Certainly, for other conditions which require larger area ratios, the narrow geometry may be more effectual.

#### The Influence of Injectant/Freestream Pressure Ratio

In considering injector performance a determination must be made of the most efficient pressure at which to deliver a given mass flux of injectant into the mixing region. In general the gas may be injected through small, high pressure jets or larger, low momentum jets. In this closely-coupled system, varying pressure ratio greatly affected the dynamics of the flow field. Pressure ratios greater than one caused rapid expansion of the helium injectant due to the steep Mach angles in the  $M = 1.7$  jet. These jet dynamics produced secondary effects on the scale of the shear layer (e.g. an increase in velocity ratio as the fluid in an underexpanded jet was accelerated). In general, focus was directed towards pressure ratios greater than or equal to one. Low pressure ratios ( $\bar{p} < 1.0$ ) were not investigated experimentally due to difficulties with unstart of the  $M = 1.7$  nozzles. The experiments and computations were conducted entirely on the wide spacing injector geometry. Static pressure ratios of  $1.0$  and  $4.0$  were investigated experimentally. Numerically, cases were run for pressure ratios of  $0.4, 1.0, 2.0$  and  $4.0$ .

Flow field survey data for  $\bar{p} = 4.0$  are presented in Figure 16. The peak helium mass fraction values in each plane are listed above the plots. Two strong differences between the  $\bar{p} = 4.0$  and  $\bar{p} = 1.0$  cases are displayed in the data. The first is the strong expansion undergone by the high pressure jet. This acted to produce higher local pressures in the air between the jets. Second, the vortical development of the high pressure jet was delayed by roughly a factor of two in distance from the injection plane. [The unique helium signature at  $\bar{x} = 0$  for the full-scale model was the result of location of grid points directly behind the wall of the injector. The  $\bar{x} = 0$  survey was actually conducted  $0.04$  inches downstream of the injection plane. The strong expansion of the high pressure jet allowed occasional measurement of helium directly behind the injector wall. The serpentine signature probably resulted from slight misalignment of the probe depending on the direction of the probe traverse, with one direction placing the probe just inside the helium/air interface.]

Planar Rayleigh data showed the spatial scale of the unsteadiness at the jet freestream interface to be comparable to that for the matched pressure case. Thus the influence of increased velocity ratio due to expansion of the jet appears minimal.

A comparison of the experimentally obtained maximum helium concentrations for the  $\bar{p} = 1.0$  and  $\bar{p} = 4.0$  cases is shown in Figure 17. As with the development of the jet, bulk mixing was delayed by a factor of two for the high pressure ratio case. The jet lift-off height comparison is made in Figure 18. It must be remembered that this data marks the height of the center of helium mass fraction and is a bulk measure of the jet trajectory. While the high pressure cases appear more attractive, consideration of the helium mass fraction contour plots shows that considerably more helium was in contact with the wall for a longer distance downstream and that separation between the bottom of the helium jet and the wall was considerably less than that obtained for the matched pressure case. Thus, the adverse heat transfer associated with the high pressure jet would be more severe in a combustor flow field. Further, the slope of the trajectory for the high pressure ratio case decayed in  $\bar{x}$



while a constant slope of 0.025 is expected for the matched pressure case after  $\bar{x} = 20$ .

A perspective plot of computational helium mass fraction contours for the  $\bar{p} = 4.0$  case is shown in Figure 19. The numerical modelling provided the opportunity to consider a low pressure ratio case as well ( $\bar{p} = 0.4$ ). This data is shown in Figure 20. These figures may be compared with the baseline case shown in Figure 2. The higher the momentum of the injectant, the less the vorticity generated by the contoured wall geometry affected the jet. This resulted in poor lift-off of the base of the jet from the surface. This is a direct result of the primary manner by which axial vorticity was generated in the flow. The vorticity was generated by fluid interaction with fixed wall geometry, and thus, to first order was fixed. Action of the vorticity upon a lower momentum jet was more effective. This behavior would not be expected for normal or angled injection from a wall where a significant portion of the energy available for mixing is derived from the dynamics of the jet itself and its interaction with the freestream. For circular sonic nozzles angled at 15 and 30 degrees to the wall, injecting helium into a Mach 3 airflow, Mays, Thomas and Schetz<sup>8</sup> showed an increase in the rate of mixing with increasing pressure ratio.

Analysis of the mixedness measure for the numerical data showed that the low pressure jet mixed to a greater extent in a more rapid manner. By  $\bar{x} = 30$ , 45% of the initial helium mass flux introduced into the flow field existed at mass fractions less than  $c_{He} = 0.05$  for  $\bar{p} = 0.4$ . At the same point, only 5% of the initial mass flux was mixed to a similar level for the high pressure case. However, normalizing by the total injectant mass flux for each case (a factor of 10), the physical mass in the system mixed to the same level was the same for the two cases. Therefore, the entrainment of air for the two cases was comparable. Consideration of the length of the  $c_{He} = 0.05$  contour level for each of the cases showed that the projected flame sheet length was similar as well.

The injectant to freestream area ratio,  $\bar{A}$ , required for complete mixing of the injectant with the freestream to a desired mixture fraction is inversely proportional to pressure ratio. It was shown that for a representative scramjet operating condition with  $\bar{p} = 1.0$ , an area ratio of  $A = 0.07$  was required. For the wide spacing case, the area would extend roughly to  $\bar{z} = 2.0, 4.0$ , and  $16.0$  for pressure ratios of  $\bar{p} = 0.4, 1.0$ , and  $4.0$  respectively. Because of the shallow far-field trajectory of the high pressure ratio case, it is expected that complete mixing of the fuel would not occur for this case until outside the domain of interest. For conditions other than that presented, the  $\bar{p} = 4.0$  case may be more effective.

Consideration of the losses for the high and low pressure ratio cases showed less entropy rise beyond that directly attributable to mixing for  $\bar{p} = 0.4$ . The strong expansion of the high pressure jet created non-isentropic compression of the air between the jets beyond that present for the low pressure case.

Based on the above results it was concluded that injectant static pressures at or below the average local static pressure in the freestream around the injection plane would be most conducive to both loss-effective mixing and strong lift-off of the jet in scramjet applications.

#### Injectant to Freestream Velocity Ratio Effects

Varying the velocity ratio acts to change the magnitude of the mean shear induced between the injectant and the freestream. As these effects were predominantly manifested in the time-fluctuating component of the flow, only experimental results are presented. Changing the velocity ratio in the numerical simulations produced only a slight broadening or narrowing of the species gradients in the mixing region. Interest in the effects of velocity ratio variations was focused on questions of performance when the velocity ratio is nominally equal to one. This case is critical because in the absence of strong shear instabilities, mixing will be primarily dependent upon the various mixing augmentation techniques applied to the flow field. Unfortunately, facility limitations did not allow delivery of helium at low enough temperatures to produce  $\bar{v} = 1.0$ . A minimum velocity ratio of  $\bar{v} = 1.12$  was obtained. The baseline cases were conducted at  $\bar{v} \approx 1.3$ . Tests were not conducted to investigate compressibility effects. In all cases the convective Mach number did not exceed 0.4.

Comparison of the survey results with those for the baseline conditions showed that very little change resulted in the flow field. Slightly higher peak helium mass fractions were obtained for the lower velocity ratio case. These are plotted and compared against the baseline case in Figure 21. The extent to which these results portray less molecular-scale mixing was not determined with confidence. Consideration of the temporally-resolved Rayleigh scattering results showed no perceptible change in the nature or scale of the unsteadiness in the flow field.

The decline in performance for the lower velocity ratio case may be related only in part to the weaker shear at the mixing interface. For  $\bar{v} = 1.12$ , the injectant to freestream static temperature ratio was 1.8. For the baseline conditions  $\bar{T} = 2.5$ . The lower velocity ratio was associated with an increase in the density of the injectant which reduced the magnitude of the baroclinic torque. Further, the vorticity generated was required to convect a jet of higher momentum flux. The poorer mixing displayed may be due to these factors as well as a decrease in shear-induced mixing.

Certainly, the decrease in bulk mixing efficiency was minor when considered on the scale of the global dynamics within the flow field. It may be concluded then, that for the limited range of velocity ratios tested, the magnitude of the mean shear established between the injectant and the freestream at the exit plane did not strongly influence the performance of the injectors. Mixing in the far-field was dominated by turbulent processes, but these processes were not driven by the average velocity ratio at the plane of injection. It is expected that the instabilities which led to the large time-fluctuating component of the flow were generated in part by localized shear associated with the dynamics of the helium jet and its interaction with the non-uniform external flow. Also, oscillatory shock interaction with a mixing interface has been shown to amplify turbulence.<sup>29</sup> The exit plane shock would be expected to display oscillations as a result of propagation through flow regions dominated by the turbulent wall boundary layer. The experimental techniques applied did not allow estimation of the relative importance of the above phenomena in generating the unsteady flow.

#### Summary of Mixing Performance for Contoured Wall Injectors with Shock-Enhanced Mixing

The difficulties in making direct comparisons of mixing performance with other injection schemes presented in the literature were addressed in detail in the review by Thomas, Schetz, and Billig.<sup>30</sup> Most notably, comparison is limited

by the wide ranging accuracy of the diagnostics in the various studies. Typically, because of the difficulty in making temporally and spatially resolved mixing measurements in high speed flows, comparisons are made on the basis of the time-mean decay of the maximum injectant concentration. It is unclear that this is an appropriate basis for comparison. The percent of fluid mixed to a given level of interest may not correlate in the near region with the rate of decay of the maximum injectant concentration. Further, temporally resolved images presented by Waitz, Marble, and Zukoski<sup>22</sup> show that the unsteady component of the flow plays a dominant role in many regions of the mixing field. The ability of the time-mean data to represent the physical phenomena must be questioned. Lack of sufficient spatial resolution further impedes the clarity of such comparisons. It is with these caveats that the results of this study should be judged against those of others in terms of mixing performance.

The time-mean decay of maximum helium concentration for all of the configurations tested experimentally are plotted in log-log form in Figure 22. The straight line portion of the data is fit with a power law proportional to  $\bar{x}^{-1.34}$  for the matched pressure cases. A power of  $n=-1.22$  was obtained when all of the experimental data were considered. In their review, Thomas, Schetz and Billig<sup>30</sup> considered a broad range of free jets, transverse jets, wall slot jets, and hybrid jets in a variety of conditions. Considered as a whole, the data they presented was grouped around a decay exponent of  $n=-0.8$ . The favorable comparison of the decay exponents obtained in this study with the gross correlation presented by Thomas, Schetz, and Billig should be judged in light of the limitations discussed above, and thus given limited weight.

## Conclusions

The effects of several salient parameters on contoured wall fuel injector performance were presented. The following conclusions are supported by both experimental and computational results.

First-order effects were noted due to the strong displacement effect of the hypersonic boundary layer which acted to modify the effective wall geometry. For narrowly-spaced injector arrays, boundary layers of scale  $\delta = 0.2$  weakened secondary flow due to the ramps and hindered shock formation in the exit plane resulting in poor time-mean convective mixing and poor jet lift-off. Zero slope jet trajectories were noted in the far field. The poor lift-off as well as close proximity of the jets to each other caused the boundary layer to be entrained into the helium injectant. This enhanced time-mean mixing to the level realized for the widely-spaced geometry. However, for scramjet applications, the higher fuel density per cross-stream distance provided by the narrow spacing, combined with weaker entrainment and poor jet penetration, would not allow complete mixing of the injectant to desired mass fraction levels.

The widely-spaced geometry was insensitive to boundary layer displacement effects for boundary layers as large as  $\delta = 0.7$ . This was due to positive interaction of the boundary flow with the ramp geometry which allowed strong secondary flow and produced regions of high momentum fluid in the corners of the troughs allowing strong baroclinic vorticity generation. Collection of the boundary layer fluid in the center of the troughs and the strong lift-off provided by the baroclinic torque isolated the jet from direct interaction with the boundary layer. It is expected that for

boundary layers greater than the vertical scale of the injectors, performance for the widely-spaced geometry will be detrimentally affected in a manner similar to the narrow geometry.

Injector performance was strongly affected by the injectant to freestream pressure ratio. This resulted from close-coupling between jet dynamics and the external flow field. For conditions representative of scramjet combustor applications, complete mixing of the fuel for the  $\bar{p} = 4.0$  case would not be expected within typical domains of interest. The axial vorticity generated by the contoured wall injectors was more effective in convecting a lower momentum injectant. Thus, pressure ratios at or below unity were judged most conducive to loss-effective mixing and strong jet penetration.

Reducing the velocity ratio between the injectant and the freestream from  $\bar{v} = 1.33$  to  $\bar{v} = 1.12$  produced only a weak decline in mixing performance. The extent to which this decline was associated with a decrease in molecular-scale mixing was not determined. In terms of the global mixing phenomena displayed in the flow field, shear-induced mixing associated with non-unity velocity ratios in the exit plane played a minor role (for the limited range of velocity ratios tested). The turbulent fluctuations which dominated the mixing in the far-field, were produced by local shear associated with the dynamics of the jet/freestream interaction, and possibly unsteady shock interaction with the mixing interface. These phenomena were not driven by small changes in injectant to freestream velocity ratio.

## Acknowledgements

Funding for this work was provided largely through NASA Grant NAG 1-842. The fundamentals of shock-enhanced mixing were developed earlier under Contract F49620-86-C-0113 administered by the Air Force Office of Scientific Research. The authors wish to thank many members of the technical staff at NASA Langley Research Center, particularly D. Bushnell, S. Robinson, M. Walsh, members of the Experimental Flow Physics Branch, and members of the Computational Methods Branch. The planar Rayleigh scattering data alluded to at several points in the discussion were the product of a collaborative effort with the Optical Spectroscopy Section of NASA Langley's Instrument Research Division. Supercomputing support was provided by the San Diego Supercomputer Center via a National Science Foundation Grant, the NASA Ames NAS facilities, the JPL/Caltech Cray, and the NASA Langley supercomputing facilities.

## References

1. Northam, G. B., Greenberg, I., and Byington, C. S., "Evaluation of Parallel Injector Configurations for Supersonic Combustion," AIAA Paper 89-2525, 1989.
2. Drummond, J. P., Carpenter, M. H., Riggins, D. W., and Adams, M. S., "Mixing Enhancement in a Supersonic Combustor," AIAA Paper 89-2794, 1989.
3. Riggins, D. W., Mekkes, G. L., McClinton, C. R., and Drummond, J. P., "A Numerical Study of Mixing Enhancement in a Supersonic Combustor," AIAA Paper 90-0203, 1990.

4. Riggins, D. W., and McClinton, C. R., "A Computational Investigation of Flow Losses in a Supersonic Combustor," AIAA Paper 90-2093, 1990.
5. Riggins, D. W., and McClinton, C. R., "Analysis of Losses in Supersonic Mixing and Reacting Flows," AIAA Paper 91-2266, 1991.
6. Hartfield, R. J., Hollo, S. D., and McDaniel, J. C., "Experimental Investigation of a Supersonic Swept Ramp Injector Using Laser-Induced Iodine Fluorescence," AIAA Paper 90-1518, 1990.
7. Davis, D. O., and Hingst, W. R., "Progress Towards Synergistic Hypermixing Nozzles," AIAA Paper 91-2264, 1991.
8. Mays, R. B., Thomas, R. H., and Schetz, J. A., "Low Angle Injection Into a Supersonic Flow," AIAA Paper 89-2461, 1989.
9. Davis, D., Hingst, W., and Porro, A., "Experimental Investigation of a Single Flush-Mounted Hypermixing Nozzle," AIAA Paper 90-5240, 1990.
10. Fuller, E. J., Thomas, R. H., and Schetz, J. A., "Effects of Yaw on Low Angle Injection into a Supersonic Flow," AIAA Paper 91-0014, 1991.
11. Fuller, E. J., Mays, R. B., Thomas, R. H., and Schetz, J. A., "Mixing Studies of Helium in Air at Mach 6," AIAA Paper 91-2268, 1991.
12. Gutmark, E., Schadow, K. C., Parr, T. P., Parr, D. M., Wilson, K. J., and Ferrell, G. B., "Enhancement of Fine-Scale Mixing for Fuel-Rich Plume Combustion," AIAA Paper 87-0376, 1987.
13. Gutmark, E., Schadow, K. C., Parr, T. P., Parr, D. M., and Wilson, K. J., "Combustion Enhancement by Axial Vortices," J. Propulsion, Vol. 5, No. 5, pp. 555-560, Sept.-Oct. 1989.
14. Samimy, M., Reeder, M., and Zaman, K., "Supersonic Jet Mixing Enhancement by Vortex Generators," AIAA Paper 91-2263, 1991.
15. Gutmark, E., Schadow, K. C., and Wilson, K. J., "Noncircular Jet Dynamics in Supersonic Combustion," J. Propulsion, Vol. 5, No. 5, pp. 529-533, Sept.-Oct. 1989.
16. Gutmark, E., Schadow, K. C., and Wilson, K. J., "Mixing Enhancement in Coaxial Supersonic Jets," AIAA Paper 89-1812, 1989.
17. Haas, F., and Sturtevant, B., "Interaction of Weak Shock Waves with Cylindrical and Spherical Gas Inhomogeneities," J. Fluid Mechanics, v. 181, pp. 41-76, 1987.
18. Marble, F. E., Hendricks, G. J., and Zukoski, E. E., "Progress Toward Shock Enhancement of Supersonic Combustion Processes," AIAA Paper 87-1880, 1987.
19. Yang, J., "An Analytical and Computational Investigation of Shock-Induced Vortical Flows with Applications to Supersonic Combustion," Ph.D. Thesis, California Institute of Technology, Pasadena, California, 1991.
19. Marble, F. E., Zukoski, E. E., Jacobs, J. W., Hendricks, G. J., and Waitz, I. A., "Shock Enhancement and Control of Hypersonic Mixing and Combustion," AIAA Paper 90-1981, 1990.
20. Marble, F. E., Zukoski, E. E., Jacobs, J. W., Hendricks, G. J., and Waitz, I. A., "Shock Enhancement and Control of Hypersonic Mixing and Combustion," AIAA Paper 90-1981, 1990.
21. Waitz, I. A., "An Investigation of Contoured Wall Injectors for Hypervelocity Mixing Augmentation," Ph. D. Thesis, California Institute of Technology, Pasadena, California, 1991.
22. Waitz, I. A., Marble, F. E., and Zukoski, E. E., "An Investigation of a Contoured Wall Injector for Hypervelocity Mixing Augmentation," AIAA Paper 91-2265, 1991.
23. Reis, V. H., and Fenn, J. B., "Separation of Gas Mixtures in Supersonic Jets," J. Chemical Physics, v. 39, no.12, 1963.
24. Chang, J. H., and Fenn, J. B., "Species Separation by Stagnation of Argon-Helium Mixtures in Supersonic Flow," Proceedings of the Seventh Rarefied Gas Dynamics Symposium, pp. 599-607, 1970.
25. Campargue, R., "The Separation Probe," Aerodynamic Separation of Gases and Isotopes, Lecture Series 82, von Karman Institute for Fluid Dynamics, 1976.
26. Carpenter, M. H., "Three-Dimensional Computations of Cross-Flow Injection and Combustion in a Supersonic Flow," AIAA Paper 89-1870, 1989.
27. Eklund, D. R., Northam, G. B., and Fletcher, D. G., "A Validation Study of the SPARK Navier-Stokes Code for Nonreacting Scramjet Combustor Flowfields," AIAA Paper 90-2360, 1990.
28. Waitz, I. A., Marble, F. E., and Zukoski, E. E., "Vorticity Generation by Contoured Wall Injectors," submitted for presentation at the AIAA/SAE/ASME 28th Joint Propulsion Meeting, Nashville, Tennessee, July 6-8, 1992.
29. Kumar, A., Bushnell, D. M., and Hussaini, M. Y., "Mixing Augmentation Technique for Hypervelocity Scramjets," J. Propulsion, pp. 514-522, Sept.- Oct. 1989.
30. Thomas, R. H., Schetz, J. A., and Billig, F. S., "Gaseous Injection In High Speed Flow," presented at the Ninth International Symposium on Air Breathing Engines, Athens, Greece, September 3-8, 1989.

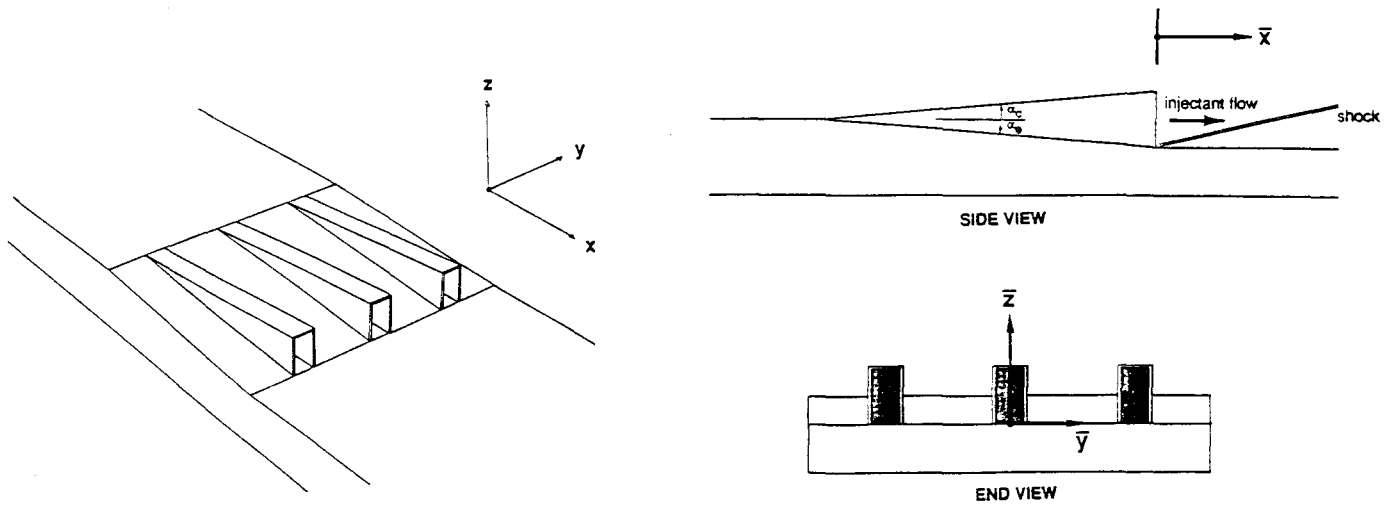


Figure 1. Diagram of contoured wall fuel injectors and definition of axes.

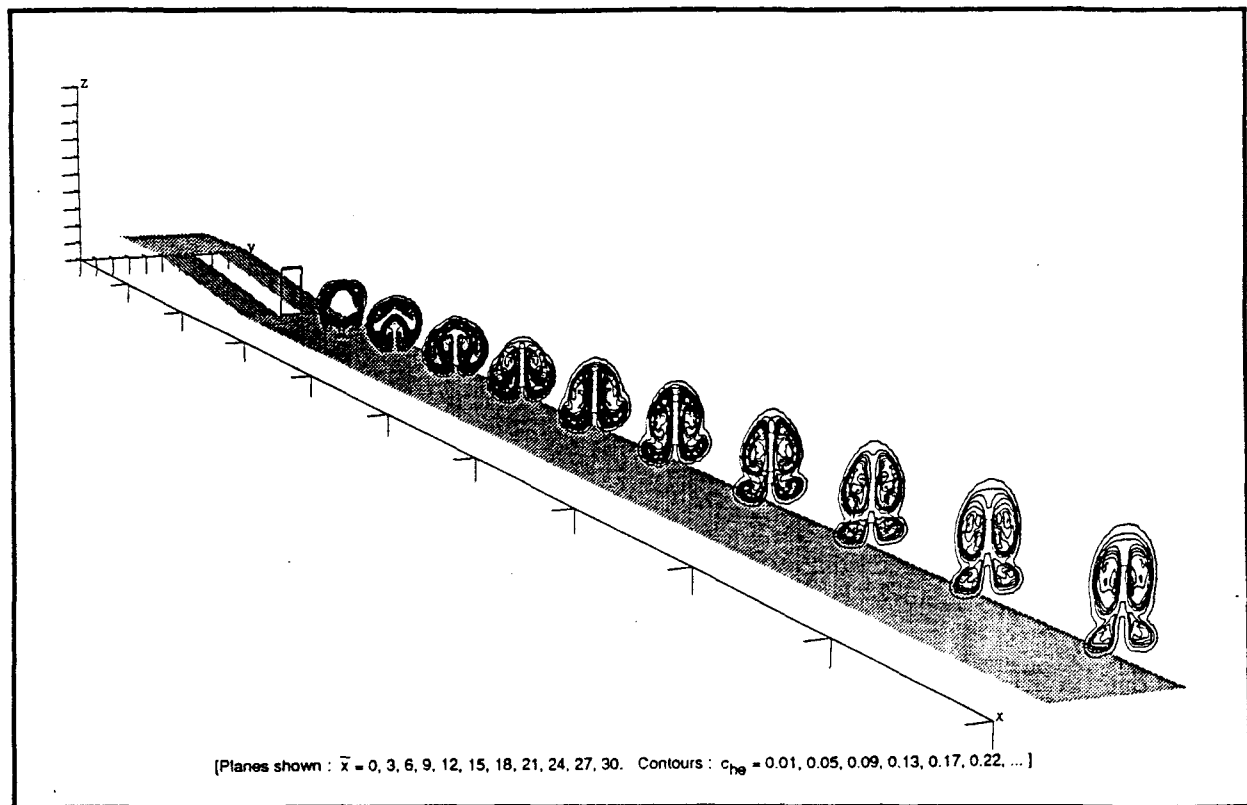


Figure 2. Contours of constant helium mass fraction.  
Wide spacing,  $\bar{\delta} = 0.2$ ,  $\bar{p} = 1.0$ ,  $\bar{v} = 1.0$  (computational).

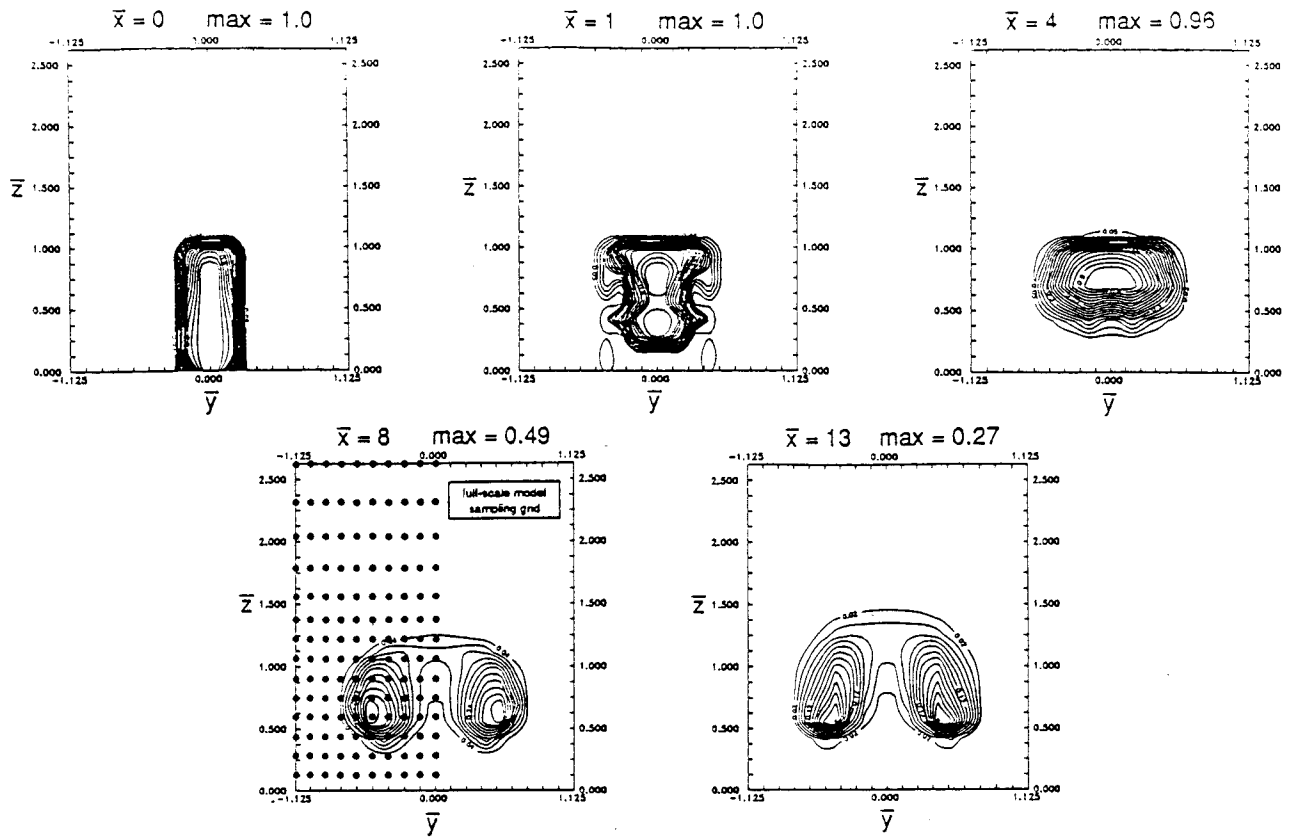


Figure 3. Helium mass fraction.  
Full-scale model, wide spacing, natural boundary layer,  $\bar{\delta} = 0.2$ ,  $\bar{p} = 1.0$ ,  $\bar{v} = 1.33$  (experimental).

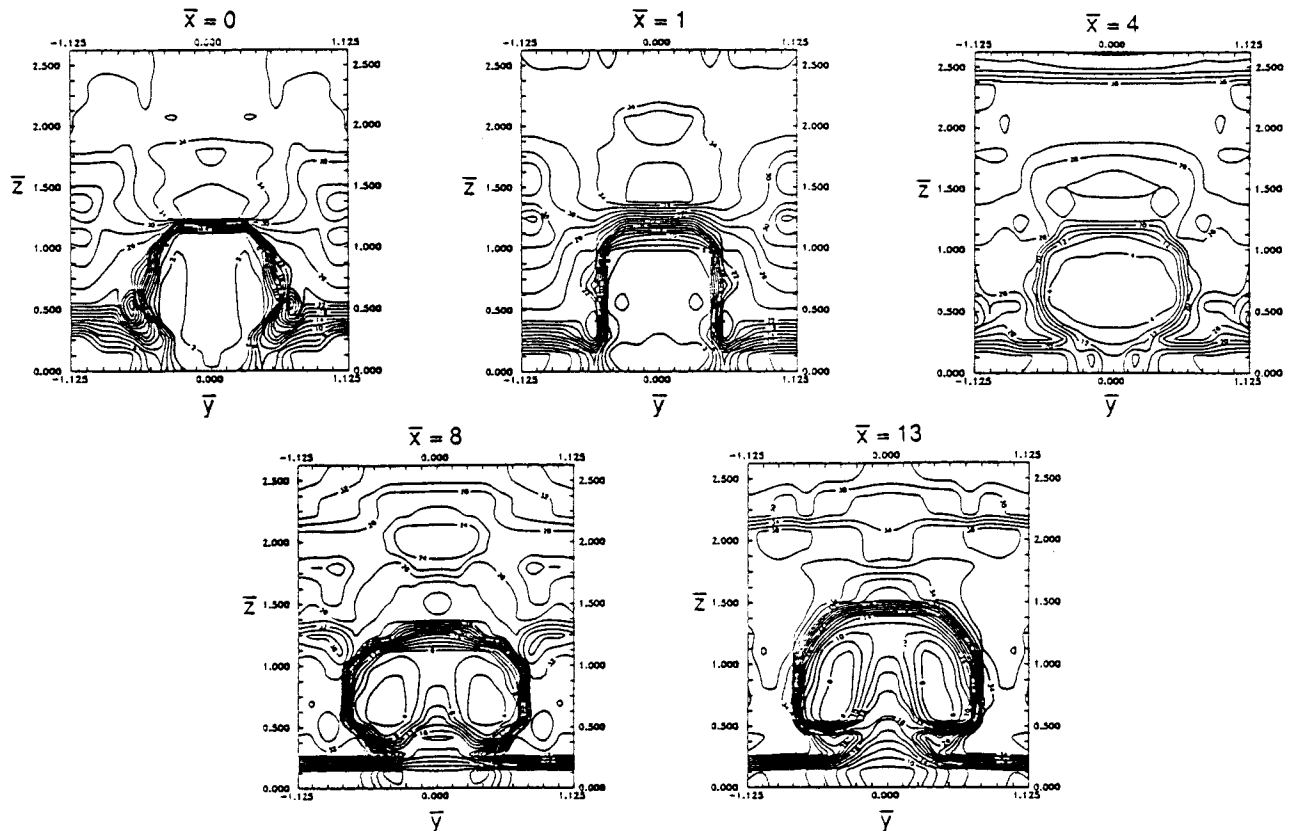


Figure 4. Pitot pressure (psia).  
Full-scale model, wide spacing, natural boundary layer,  $\bar{\delta} = 0.2$ ,  $\bar{p} = 1.0$ ,  $\bar{v} = 1.33$  (experimental).

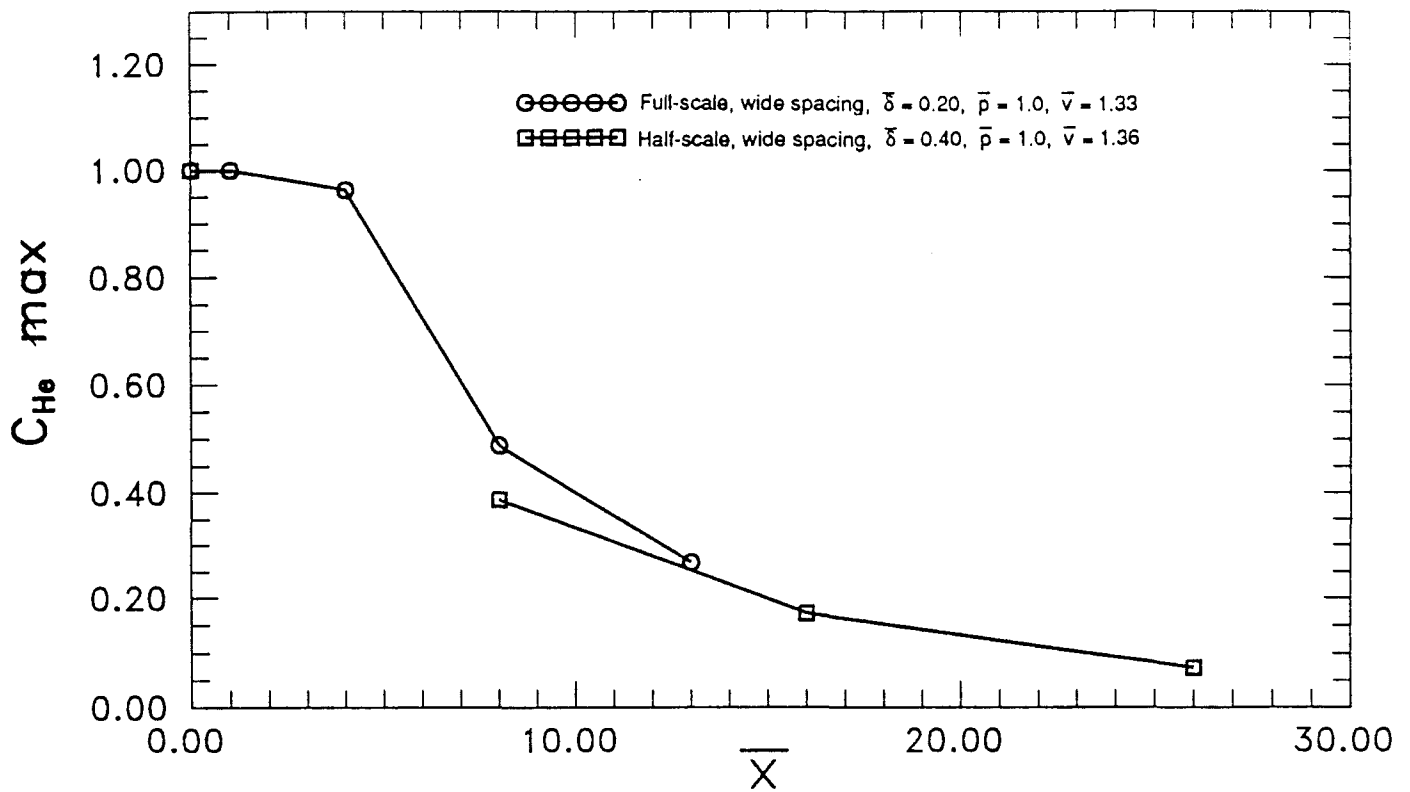


Figure 5. Decay of maximum helium mass fraction.  
Wide spacing, natural boundary layer,  $\bar{p} = 1.0$  (experimental).

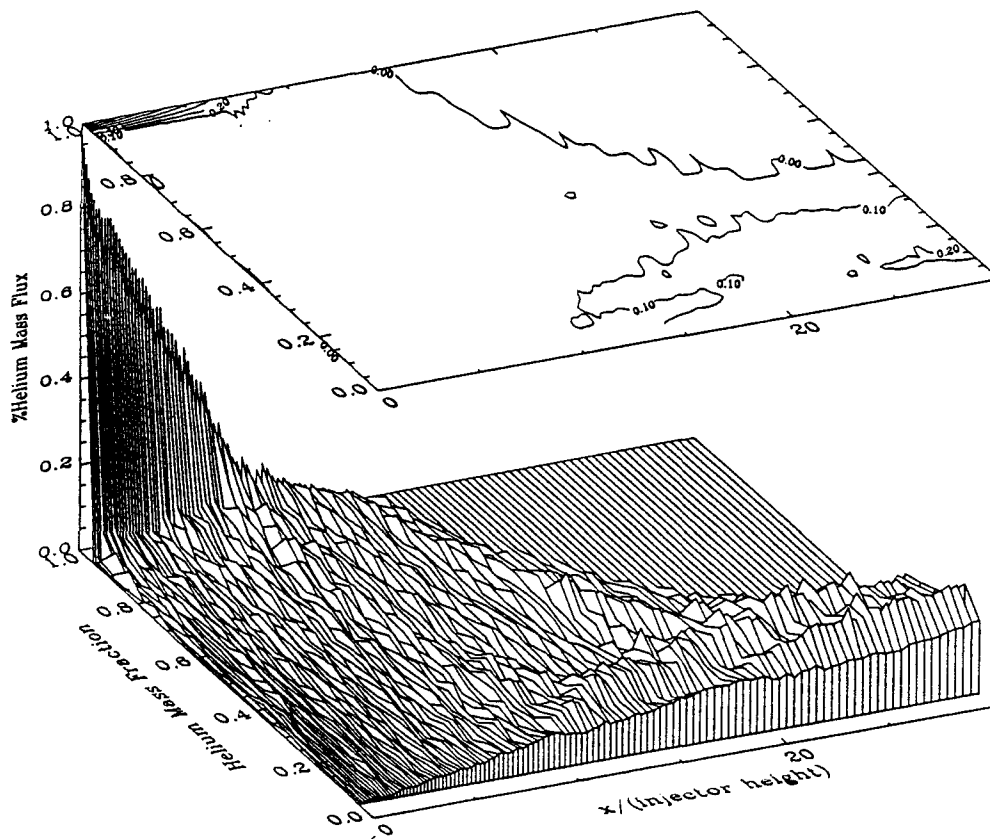


Figure 6. Mixedness measure. Wide spacing,  $\bar{\delta} = 0.2$ ,  $\bar{p} = 1.0$ ,  $\bar{v} = 1.0$  (computational).

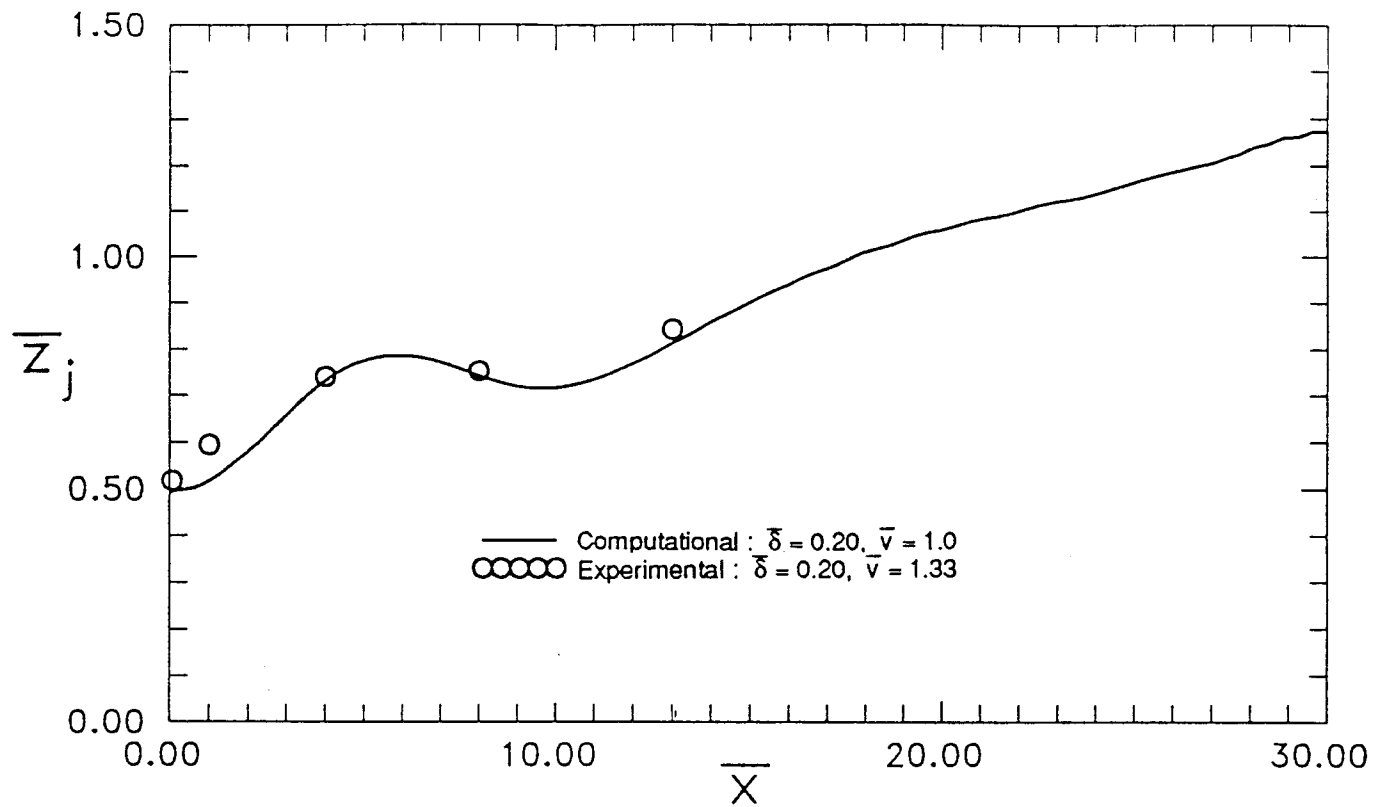


Figure 7. Jet lift-off. Wide spacing, thin boundary layer,  $\bar{p} = 1.0$ .

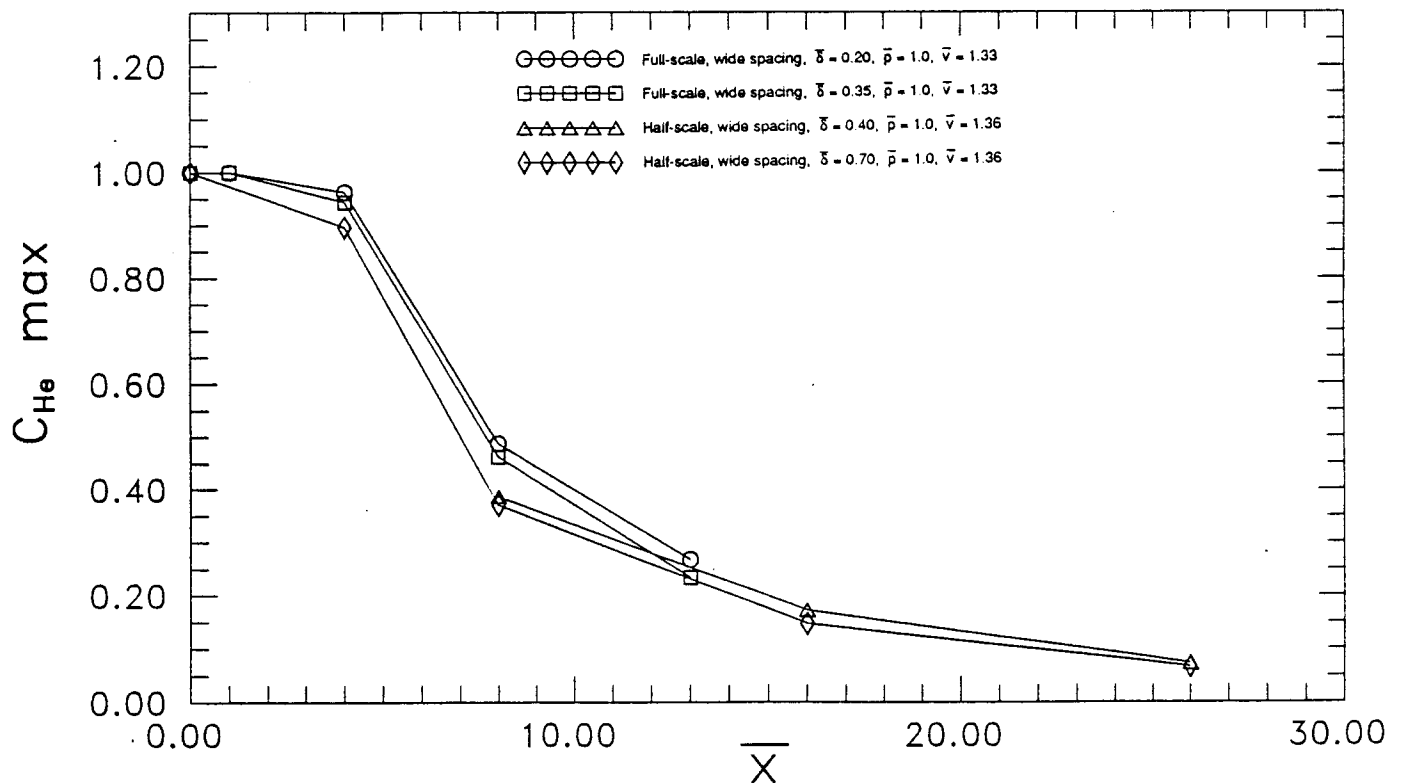


Figure 8. Decay of maximum helium mass fraction for the widely-spaced injector array with boundary layers of various heights (experimental).



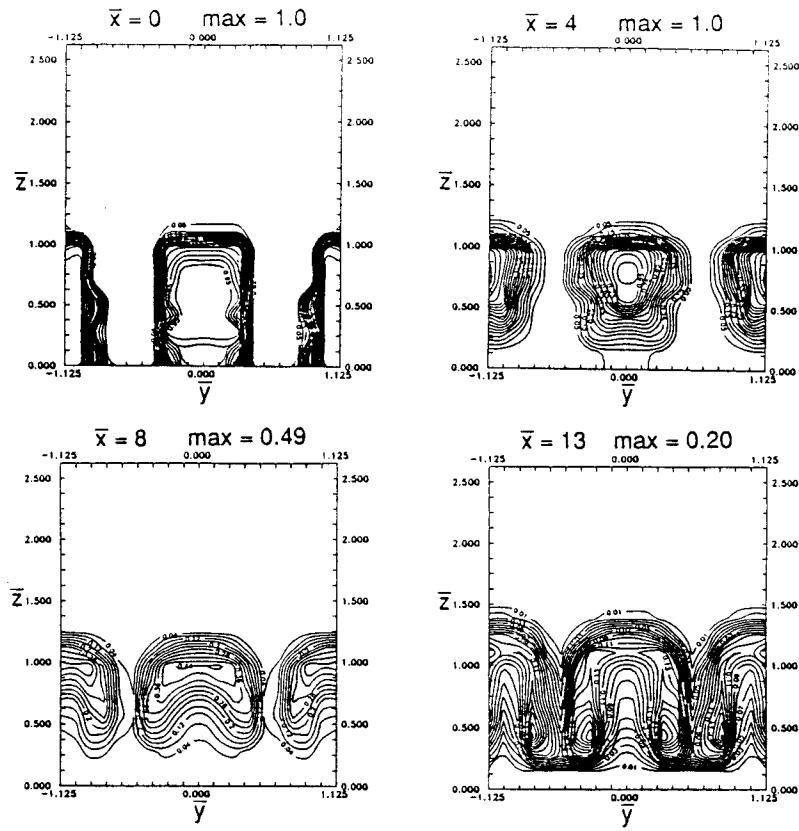


Figure 9. Helium mass fraction.  
Full-scale model, narrow spacing, natural boundary layer,  $\bar{\delta} = 0.2$ ,  $\bar{p} = 1.0$ ,  $\bar{v} = 1.28$  (experimental).

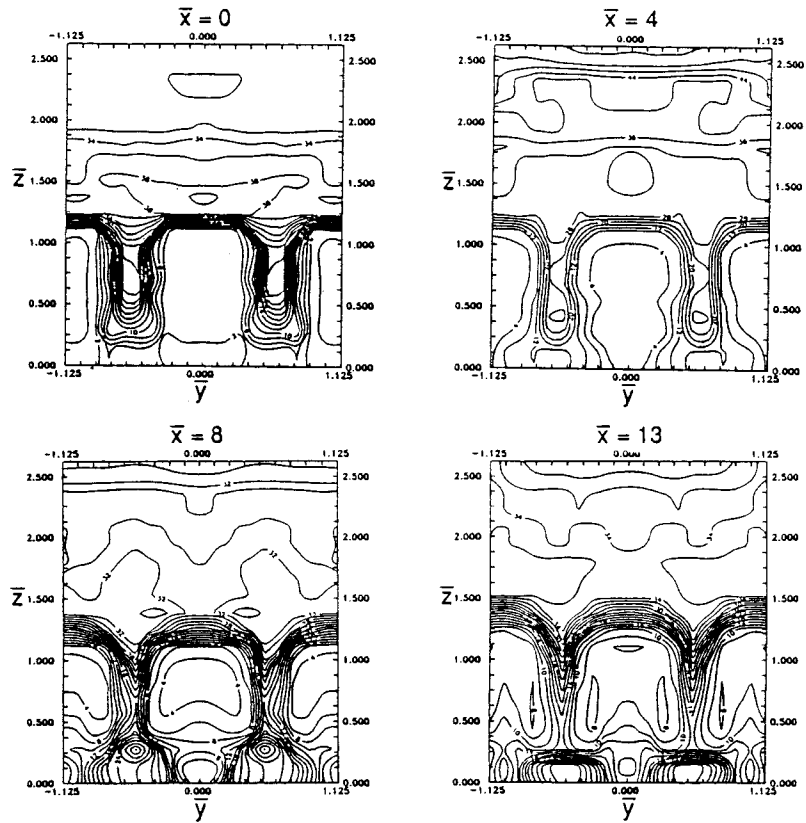


Figure 10. Pitot pressure (psia).  
Full-scale model, narrow spacing, natural boundary layer,  $\bar{\delta} = 0.2$ ,  $\bar{p} = 1.0$ ,  $\bar{v} = 1.28$  (experimental).

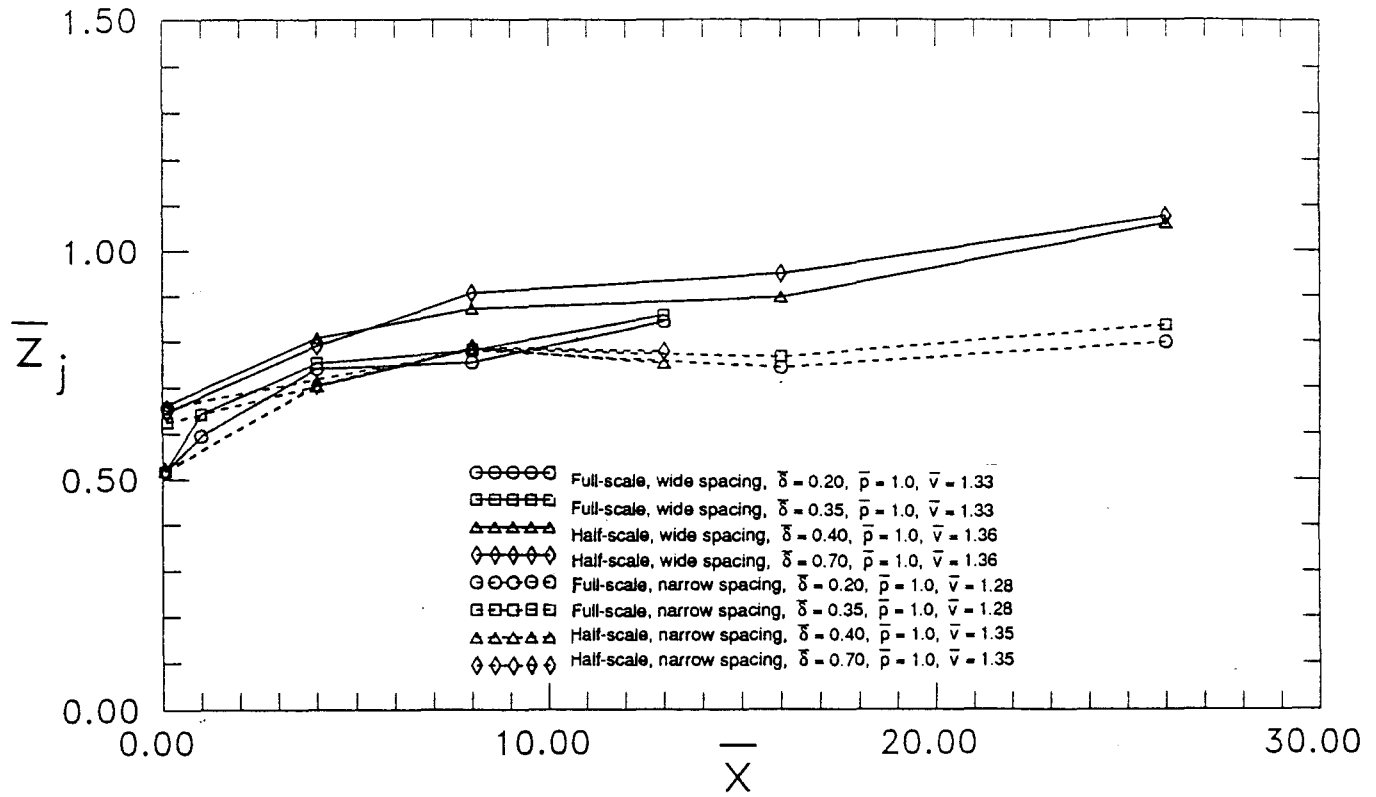


Figure 11. Jet lift-off. Boundary layer and injector spacing effects (experimental).

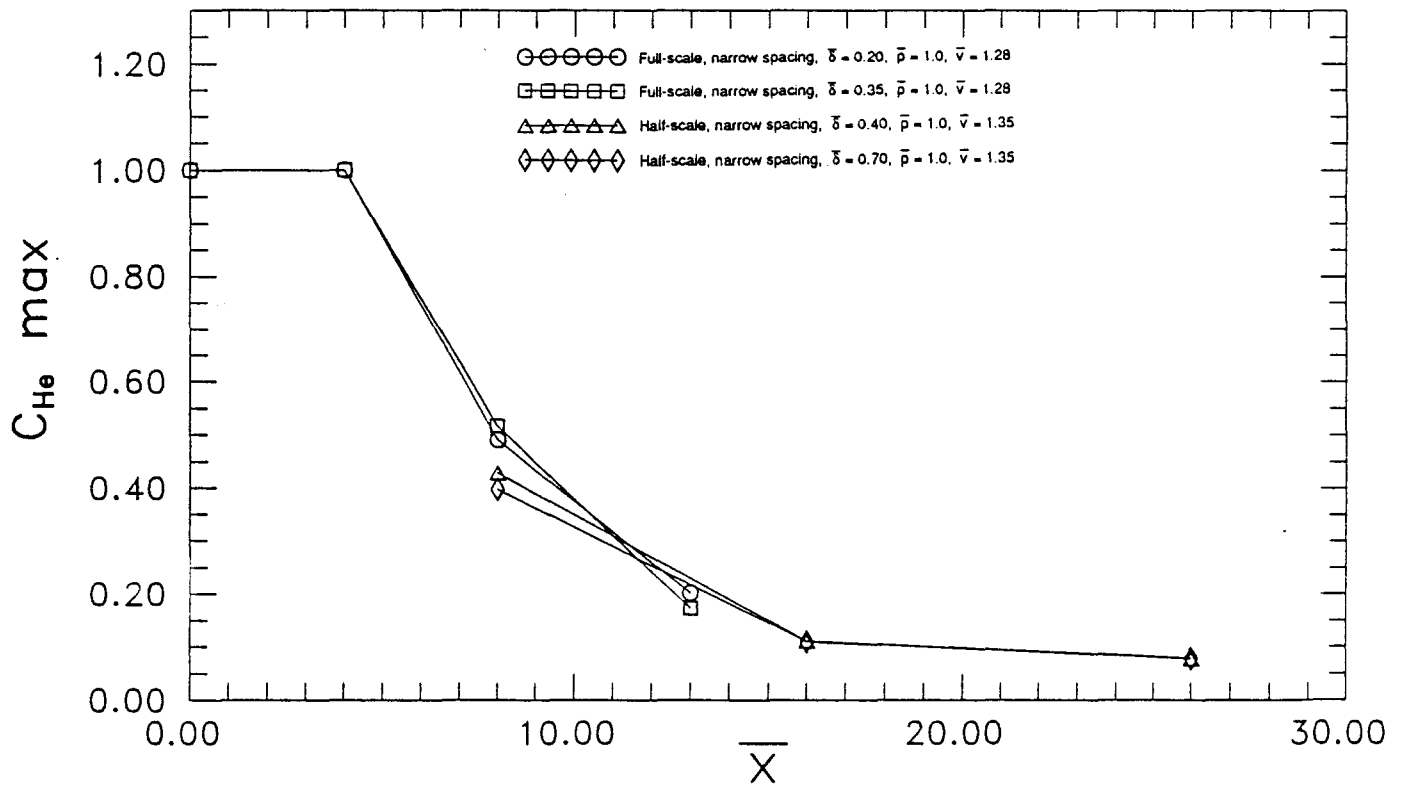


Figure 12. Decay of maximum helium mass fraction for the narrowly-spaced injector array with boundary layers of various heights (experimental).

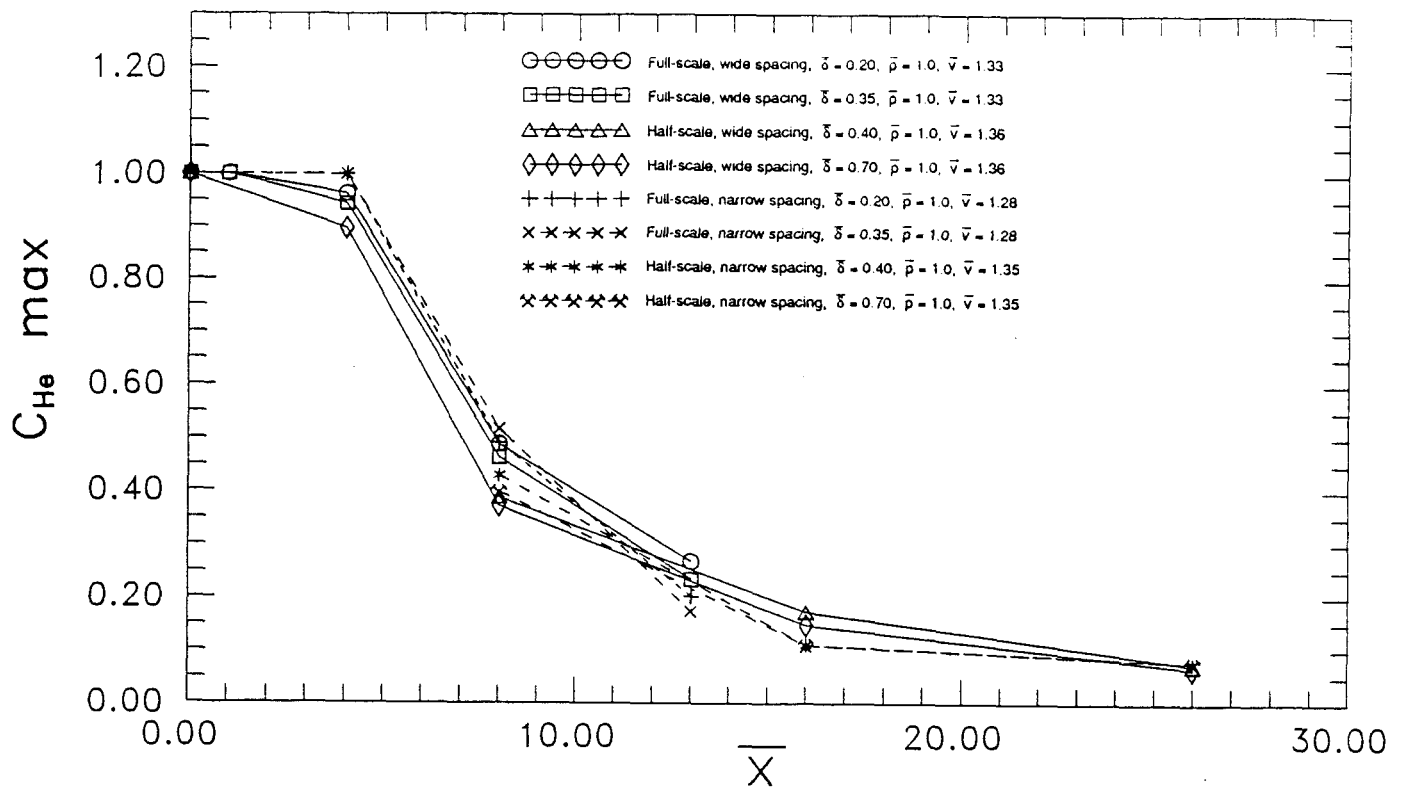


Figure 13. Decay of maximum helium mass fraction for various spacings and boundary layer thicknesses (experimental).

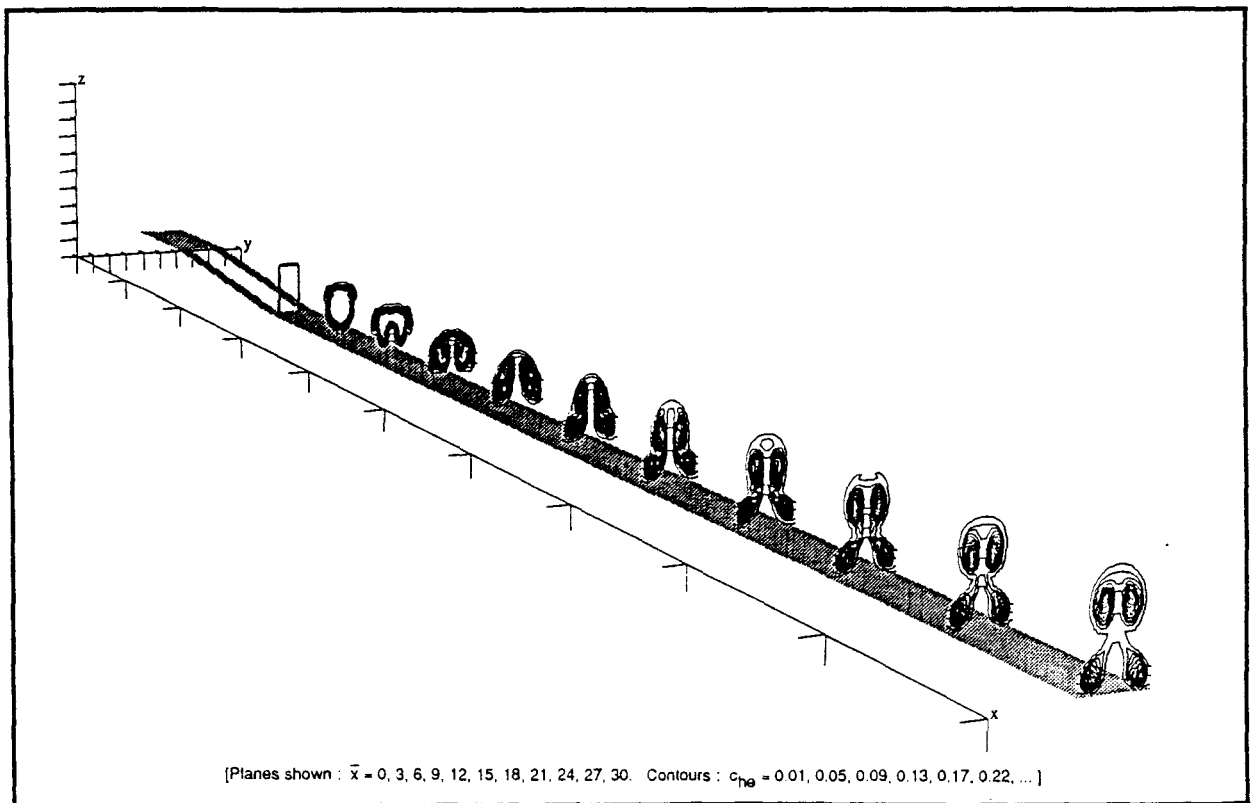


Figure 14. Contours of constant helium mass fraction.  
Narrow spacing,  $\bar{\delta} = 0$  (inviscid b.c.),  $\bar{p} = 1.0$ ,  $\bar{v} = 1.0$  (computational).

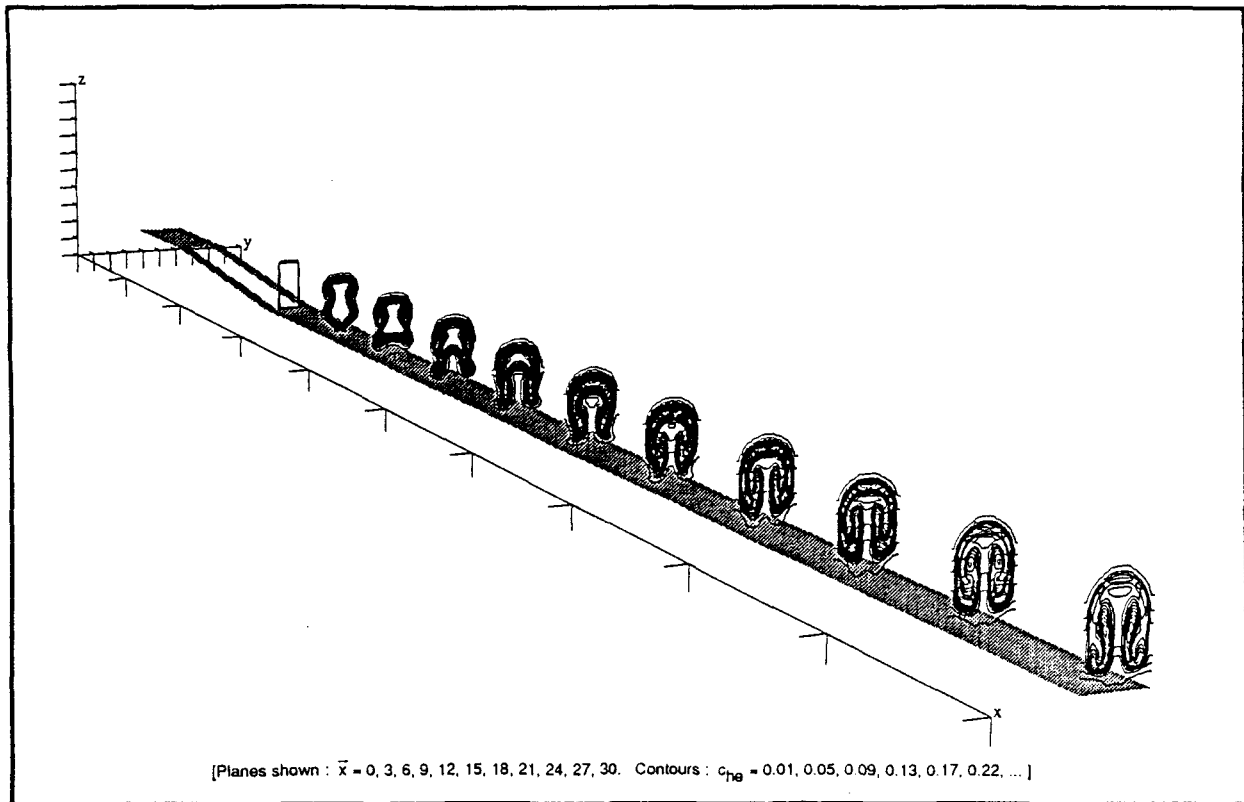


Figure 15. Contours of constant helium mass fraction.  
Narrow spacing,  $\bar{\delta} = 0.2$ ,  $\bar{p} = 1.0$ ,  $\bar{v} = 1.0$  (computational).

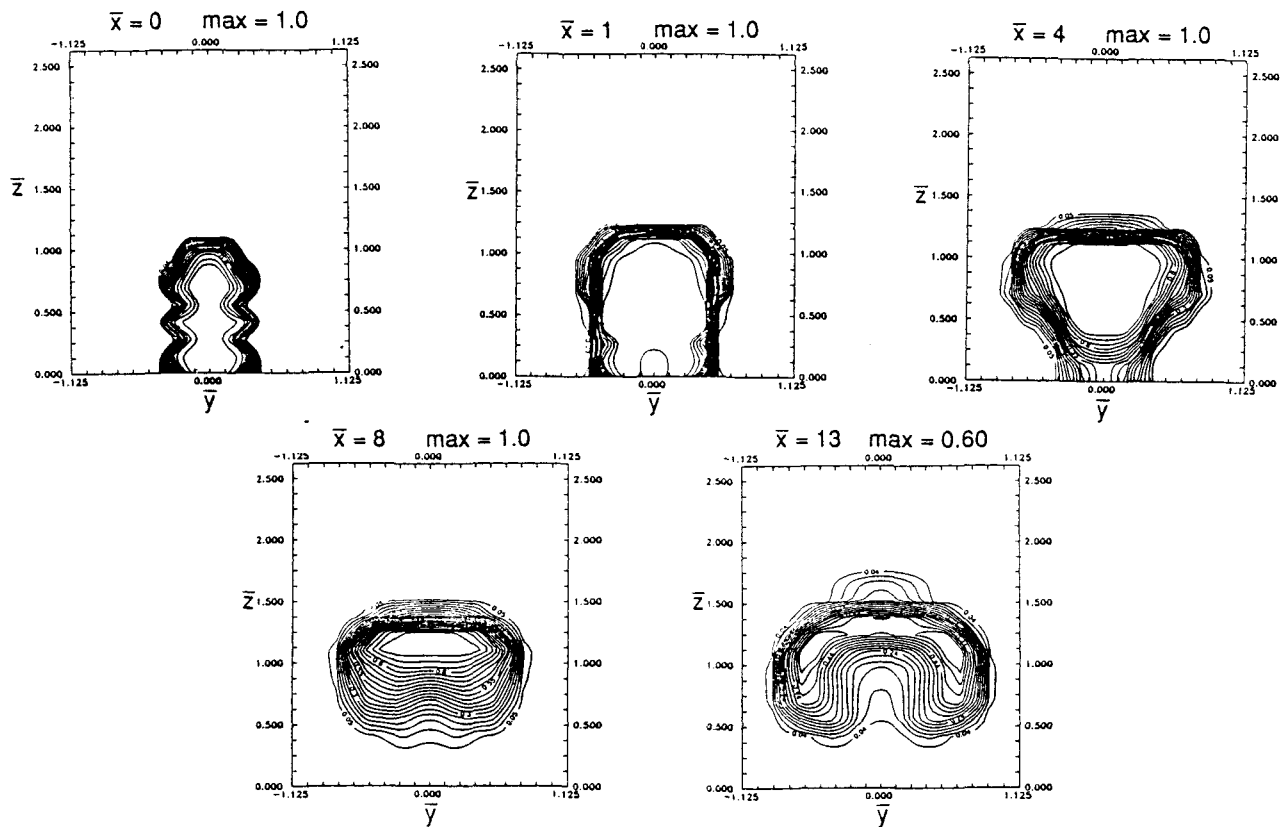


Figure 16. Helium mass fraction.  
Full-scale model, wide spacing, natural boundary layer,  $\bar{\delta} = 0.2$ ,  $\bar{p} = 4.0$ ,  $\bar{v} = 1.27$  (experimental).

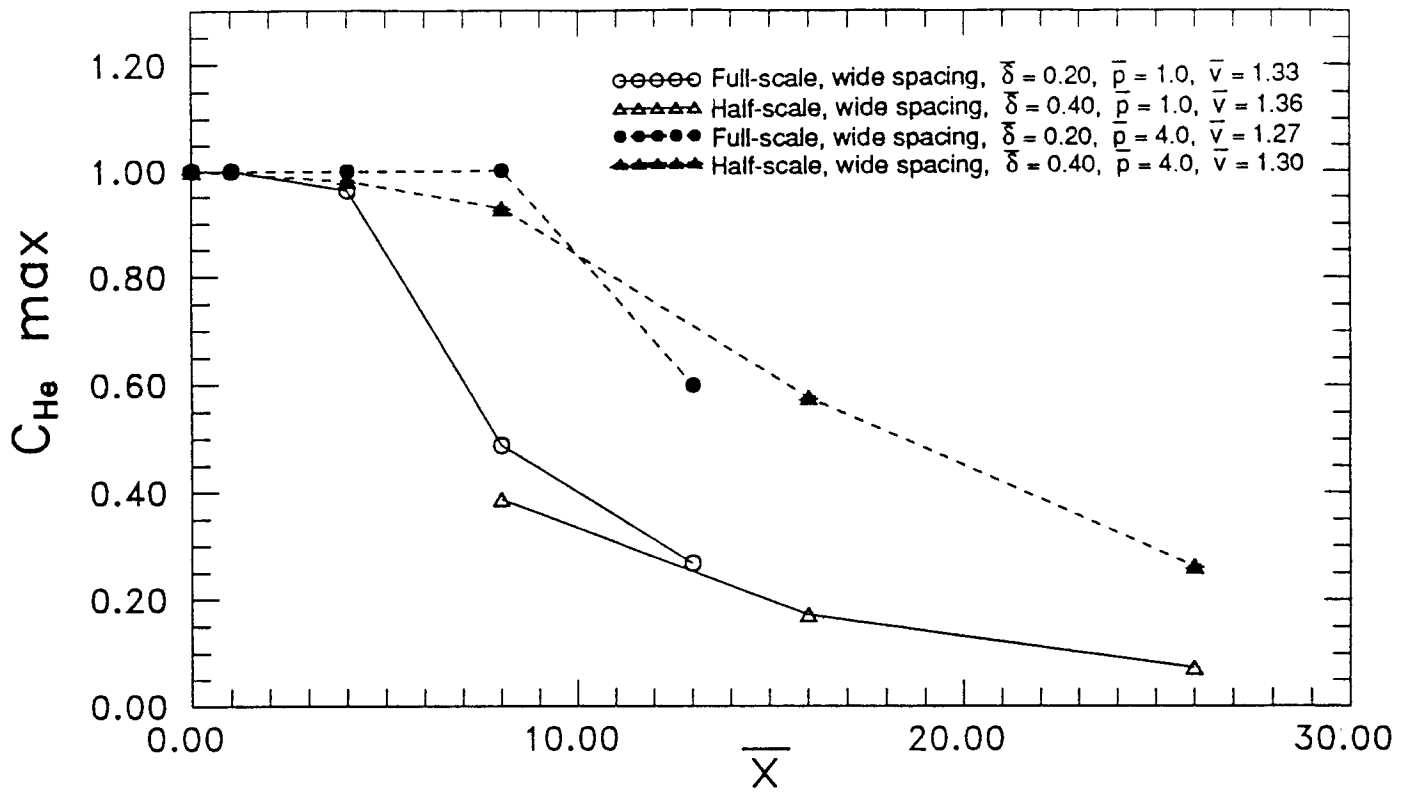


Figure 17. Decay of maximum helium mass fraction: pressure ratio effects (experimental).

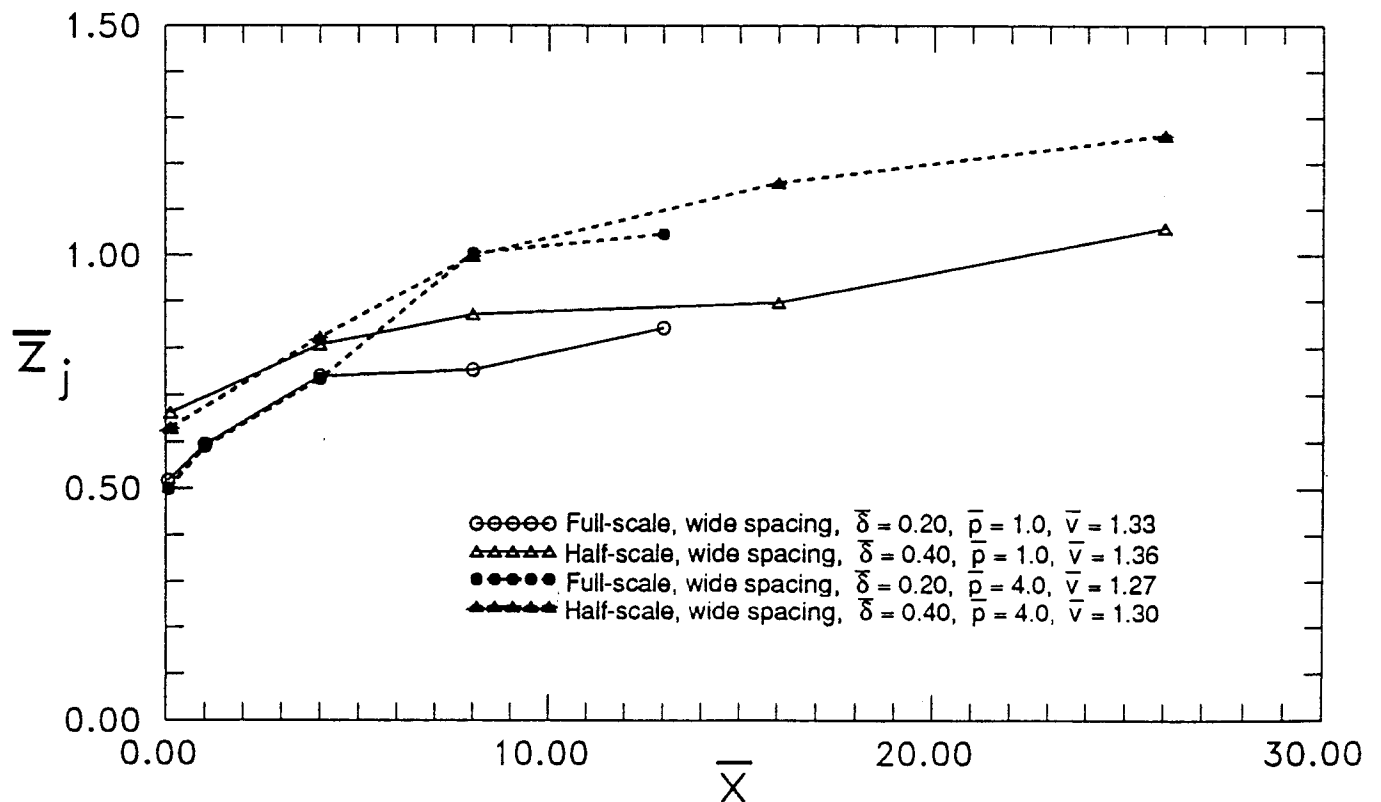


Figure 18. Jet lift-off: pressure ratio effects (experimental).

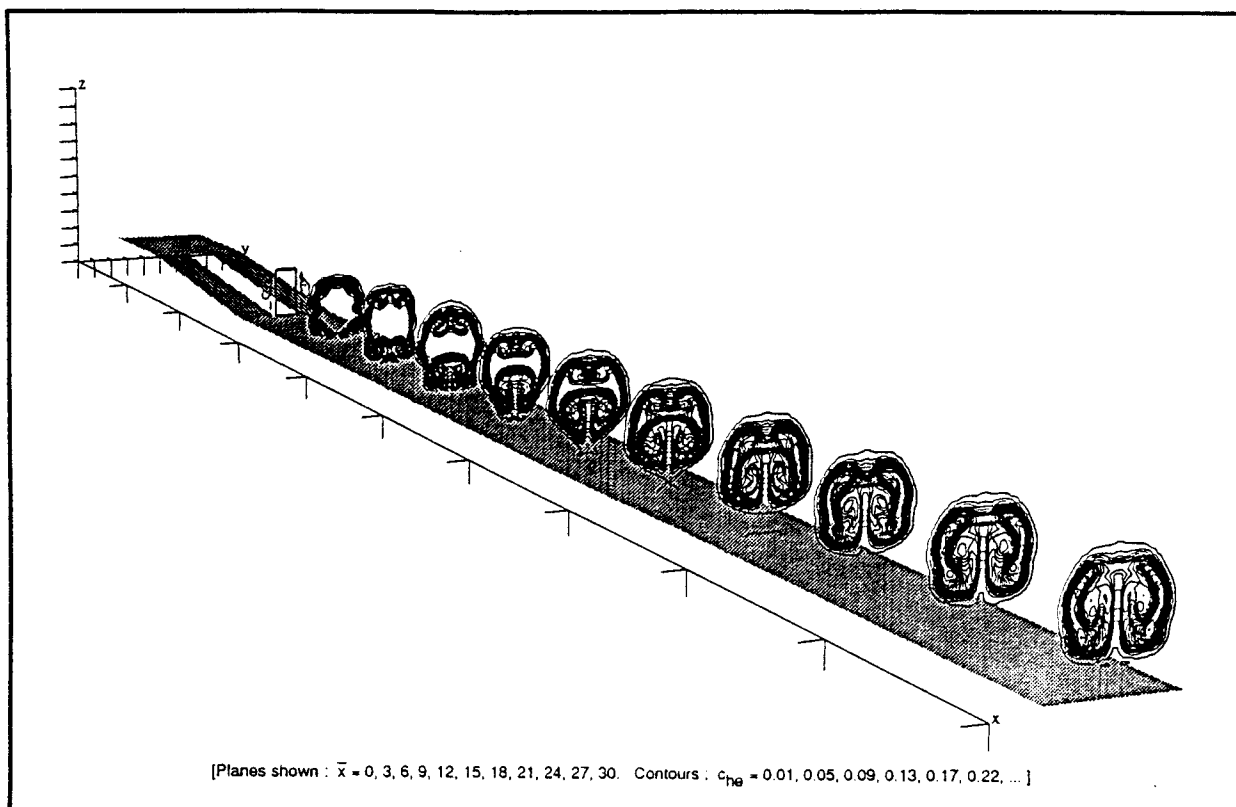


Figure 19. Contours of constant helium mass fraction.  
Wide spacing,  $\bar{\delta} = 0.2$ ,  $\bar{p} = 4.0$ ,  $\bar{v} = 1.0$  (computational).

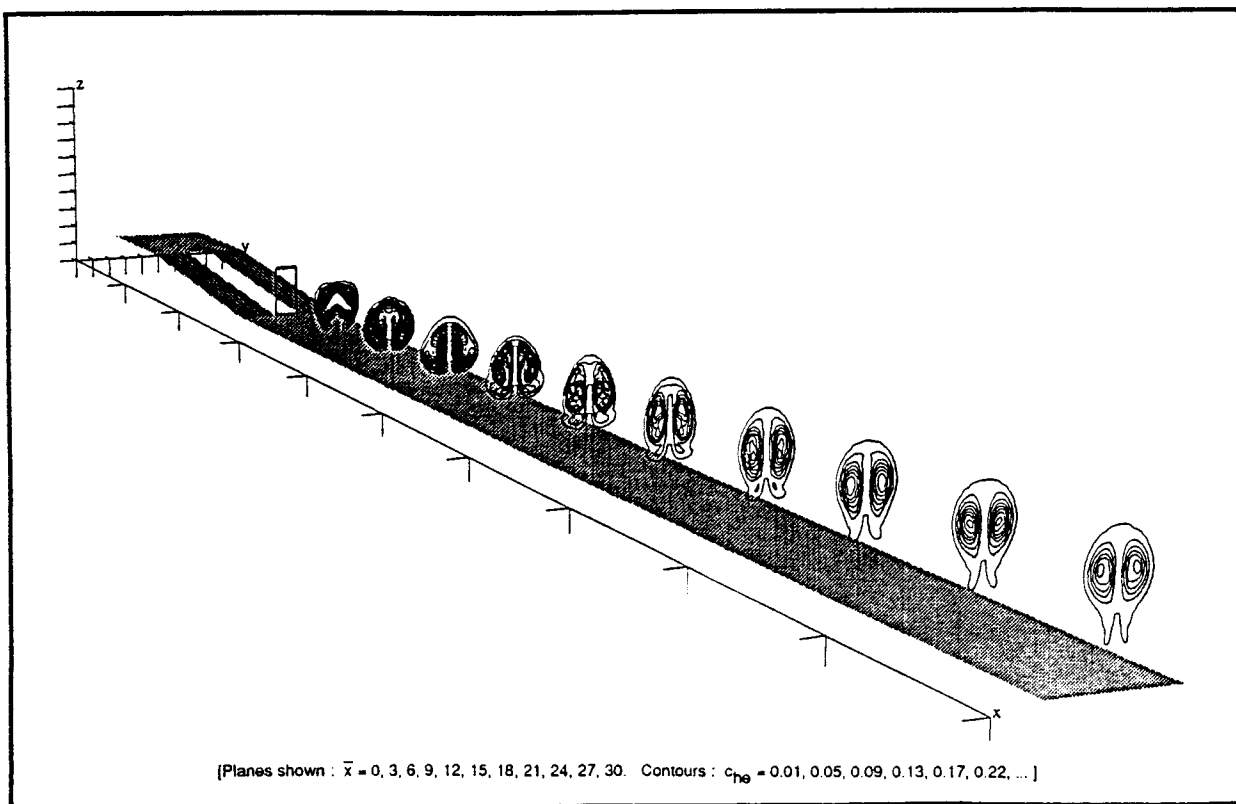


Figure 20. Contours of constant helium mass fraction.  
Wide spacing,  $\bar{\delta} = 0.2$ ,  $\bar{p} = 0.4$ ,  $\bar{v} = 1.0$  (computational).

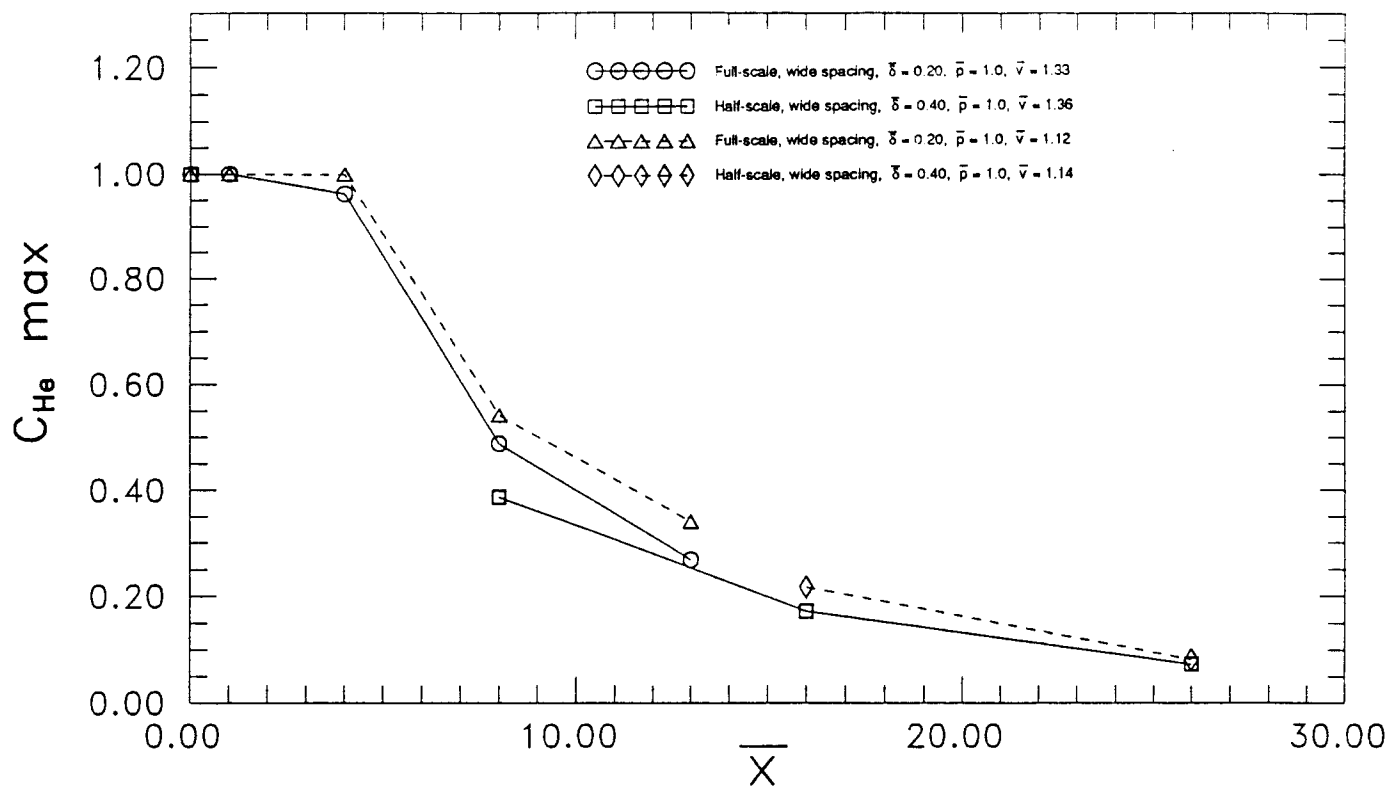


Figure 21. Decay of maximum helium mass fraction: velocity ratio effects (experimental).

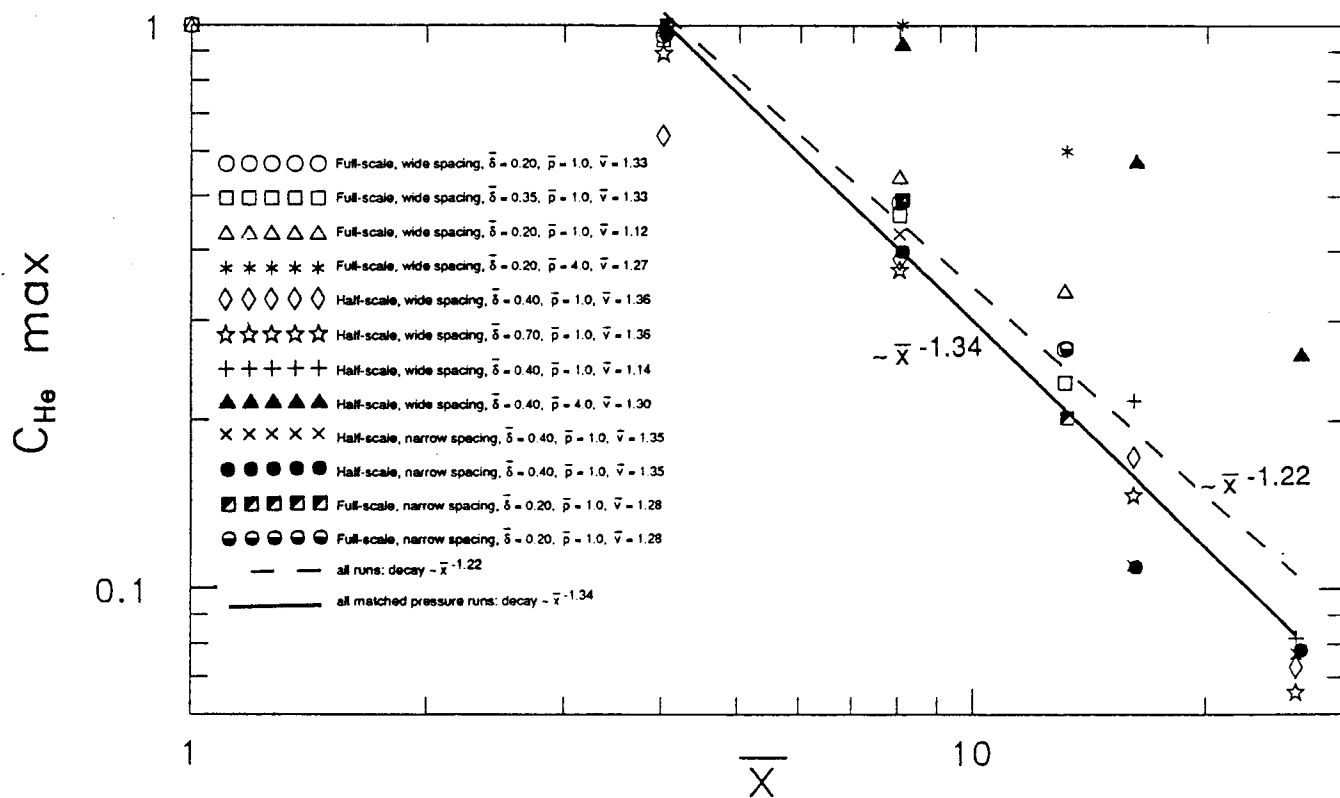


Figure 22. Decay of maximum helium concentration for experimental data.